J. Fluid Mech. (2022), *vol*. 949, A39, doi:10.1017/jfm.2022.781

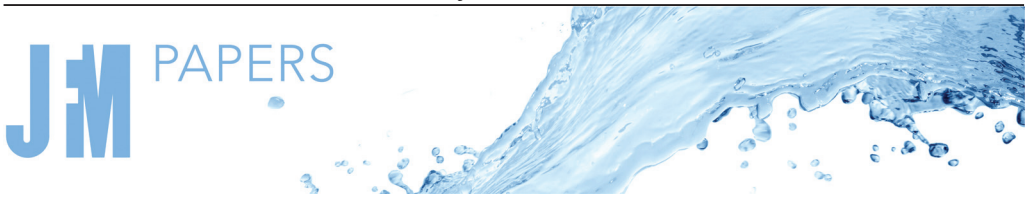

Flow–structure interaction of a starting jet through a flexible circular nozzle

Daehyun Choi[1] **and Hyungmin Park**[1,2],†

[1]Department of Mechanical Engineering, Seoul National University, Seoul 08826, Korea

[2]Institute of Advanced Machines and Design, Seoul National University, Seoul 08826, Korea

(Received 9 February 2022; revised 1 July 2022; accepted 5 September 2022)

In the present study, the flow–structure interaction of a starting jet through a flexible nozzle is experimentally investigated, with a focus on the optimal flexibility for thrust generation. Water slug is impulsively accelerated through a cylindrical nozzle, fabricated with silicone rubber of varying flexibility. In general, the flexible nozzle modifies the vortical structure of the jet and augments the thrust of the starting jet. The measurement of nozzle surface deformation revealed that a back-and-forth wave propagation on the nozzle surface is responsible for the jet-vortex evolution augmenting the thrust generation. Combining the hydrodynamic conservation equations and the linearized shell theory, we also formulated the governing equations, dominated by two relevant dimensionless parameters: the effective acceleration time of the jet (Π_0) and the effective nozzle stiffness (Π_1). Asymptotic analysis of the equation showed that the dimensionless wave speed ($\hat{c}$) is expressed as $\hat{c} = (\Pi_0^2\Pi_1/2)^{0.5}$, and the jet momentum is maximized at $\hat{c} = \hat{c}_{crit}$ ($\simeq 3.0$), the condition at which the release of elastic energy stored during nozzle contraction to the jet is synchronized with the instant of termination of jet acceleration. While $\hat{c} = \hat{c}_{crit}$, the achievable maximum jet velocity decreases with the effective acceleration time of the jet (Π_0), which is attributed to the reduced speed of the surface wave by the flow inside the nozzle.

Key words: flow–structure interactions, jets

1. Introduction

A starting jet is ubiquitous in diverse fluid applications that require the transport of fluid energy to fulfil various purposes, such as the cleaning process of bag filters (Li *et al.* 2016) and pulsed-jet propulsion of aircraft (Garnier 2015), underwater vehicles (Linden 2011; Renda *et al.* 2015) and natural organisms such as squid (Packard 1969; Gosline &

† Email address for correspondence: hminpark@snu.ac.kr

DeMont 1985; Weymouth & Triantafyllou 2013), salp (Sutherland & Madin 2010) and jellyfish (Park *et al.* 2014; Fang *et al.* 2017). In the biomedical field, blood influx to the atrium through the heart valve (Mittal 2018) and the transmission of viral droplets through sneezing (Bourouiba, Dehandschoewercker & Bush 2014; Mittal, Ni & Seo 2020) can be understood through the dynamics of a starting jet.

The flow induced by a starting jet can be characterized in terms of the hydrodynamic impulse, contributed by fluid inertia and pressure difference, because it is directly related to not only thrust generation but also the entrainment (mixing) of the ambient fluid (Krueger & Gharib 2003; Krieg & Mohseni 2013). Because the momentum flux is an integration of $\rho_f u_e^2$ (where u_e is the jet-exit velocity and ρ_f is the fluid density) on the jet-exit plane during a specified time duration, it is generally affected by the jet generator (e.g. piston and impeller), in particular for a rigid nozzle or steady jetting condition. On the other hand, the contribution of the pressure difference ($p - p_\infty$, where p_∞ is the ambient pressure) is affected by various factors (Krueger & Gharib 2003; Krieg & Mohseni 2013; Gao *et al.* 2020). Because the jet-exit pressure is closely related to the pinch-off dynamics of the vortex ring and the subsequent entrainment process, previous studies used the formation number (F), defined as the ratio of piston stroke to nozzle diameter, to understand it. Considering the formation number as a characteristic time scale, it was suggested that the fully grown primary vortex ring pinches off the nozzle tip at a critical value of $F \simeq 4.0$, which entrains the ambient fluid and increases the pressure rise at the exit, thereby maximizing the total thrust normalized by the momentum flux (Gharib, Rambod & Shariff 1998; Krueger & Gharib 2003). At the same formation number, on the other hand, a faster acceleration of the jet results in a higher thrust production (Krueger & Gharib 2003), and Gao *et al.* (2020) mentioned that the pressure rise is altered by transient jet evolution such as the growth of the primary vortex and the deceleration process of the jet. Meanwhile, Krieg & Mohseni (2013) measured the increase in the impulse from a converging nozzle by 70 % compared with a circular cylinder nozzle and explained that the radial velocity contributes to the rise in pressure at the jet exit using the potential flow theory. Meanwhile, Limbourg & Nedić (2021*a*,*b*) proposed the modified slug-flow model, which can account for flow contraction at the nozzle exit.

In terms of a jet-propelled vehicle (or robot), it was reported that pulsed-jet propulsion is more efficient than that by a steady jet because of the added mass and entrainment effect (Siekmann 1963; Krueger & Gharib 2003; Dabiri 2009; Bujard, Giorgio-Serchi & Weymouth 2021), which depends on the formation number (Moslemi & Krueger 2010; Nichols & Krueger 2012; Whittlesey & Dabiri 2013), jet acceleration (or deceleration) (Krieg & Mohseni 2015) and Reynolds number (Moslemi & Krueger 2011). Despite these achievements, studies concerned with maximizing thrust are quite lacking. When the nozzle through which a propulsive jet flow is issued is rigid, the generated impulse is directly determined by the piston movement and nozzle geometry; however, if the nozzle material is sufficiently flexible so that it can interact with the jet, the fluid–structure interaction will significantly affect the generated impulse as well as the efficiency.

As a method to control the hydrodynamics of a moving body, on the other hand, many nature-inspired researches have investigated the fluid–structure interaction in the flow over a flexible (compliant) surface (Triantafyllou, Triantafyllou & Grosenbaugh 1993; Kang *et al.* 2011; Marais *et al.* 2012; Park *et al.* 2012, 2016; Dewey *et al.* 2013; Quinn, Lauder & Smits 2014, 2015; David, Govardhan & Arakeri 2017; Medina & Kang 2018). In common, they reported that a certain level of flexibility enhances thrust generation or power efficiency of a flapping wing and fin model, which has been explained

through the alignment of shed vortices with surface deformation. Dewey *et al.* (2013) showed that thrust generation and propulsive efficiency of a flexible pitching panel are maximized when the dimensionless pitching frequency (Strouhal number, St) is in the range $0.2 < St < 0.25$ (where $St = f_p A_p/u_\infty$, in which f_p is the pitching frequency, A_p is the pitching amplitude and u_∞ is the free-stream velocity) and matches the natural (structural) frequency of the panel. Park *et al.* (2012, 2016) explained the optimal flexibility for thrust generation in terms of the phase lag ($= \pi/2$) between the pitching angle, i.e. the condition of vortex shedding, and the rotation of the trailing edge owing to the flexibility. Li, Jaiman & Khoo (2021) reported that the flow-induced oscillation of a flexible membrane enhances lift generation by extending the leading-edge vortices, and a transition of vibrational modes appears owing to the frequency lock-in between the natural frequency of the membrane and vortex-shedding frequency. In addition, a flexible flapping foil is known to suppress asymmetric vortex shedding, inhibiting deflection of the propulsive jet (Marais *et al.* 2012).

Despite the advances in understanding the role of flexible surfaces in flow control, its application is confined to undulating appendages like wing, fin and flag. Furthermore, the effect of flexibility on jet flow requires a more fundamental investigation. For example, Dabiri & Gharib (2005) reported that the circulation of the leading vortex ring is enhanced by forcing the active shrinkage of a circular nozzle exit during the operation of the starting jet, which decreases the kinetic energy of the vortex and thereby sustains the vorticity supply. Das, Govardhan & Arakeri (2018) showed that a flexible flap attached to the tip of a two-dimensional slit increases the jet impulse two times by enhancing the circulation of jet vortices. Also, Jung, Song & Kim (2021) recently showed that the eversion of an elastic sheet installed at the nozzle exit enhances the impulse of a starting jet, which increases with bending rigidity. Dabiri (2009) suggested that a living structure (such as the human heart and jetting marine animals) operates under specific optimal conditions in terms of vortex formation. However, the governing parameter (i.e. formation number only) obtained for the ideal case (i.e. piston experiment) has a limitation in terms of explaining the different strategies used universally. Furthermore, a physical model for optimal flexibility, beyond a qualitative description, needs to be developed based on fluid–structure interaction analysis of unsteady jet-flow evolution. Indeed, most previous studies tend to simply conclude that a flexible surface performs better than a rigid one without a systematic quantification of the relevant parameters.

It would be helpful to briefly summarize the previous studies of flow inside a flexible tube (Lin & Morgan 1956; Kraus 1967; Païdoussis & Denise 1972; Chen & Rosenberg 1974; Païdoussis 1998), which has gained more attention than jet flow. The natural frequency and vibration mode of an immersed thin flexible tube can be predicted using the thin elastic shell theory, together with hydrodynamic equations (Lin & Morgan 1956; Kraus 1967). While the inertia and acoustic couplings between the flexible tube and viscous fluid flow significantly affect the frequency and wavenumber of the resulting wave on the tube (dispersion relation), each contribution can be characterized by the mass (χ) and speed ratio (c_{sr}). The mass ratio is defined as $\chi = \rho_f R/(\rho_s h)$, where ρ_s, h and R are the tube density, wall thickness and tube radius, respectively, and the speed ratio (c_f/c_s) is the ratio of the speed of sound in fluid (c_f) to the wave speed (c_s) on the tube surface (Lin & Morgan 1956; Chen & Rosenberg 1974; Païdoussis 1998). Furthermore, the flow inside the flexible tube could lead to self-excited oscillation of various modes and frequencies (Bertram, Raymond & Pedley 1991; Heil 1997; Kumaran 1998; Heil & Waters 2006; Heil & Boyle 2010; Whittaker *et al.* 2010; Paak, Païdoussis & Misra 2013; Siviglia & Toffolon 2014; Stewart 2017; Zhang, Luo & Cai 2018; Abdelbaki, Paidoussis &

Misra 2020; Podoprosvetova & Vedeneev 2022). When one end of the tube is clamped and the other is free, similar to the present condition, steady flow with a bulk velocity of u_b excites periodic, multimode or chaotic vibration at a specific velocity ratio, $u_r = u_b/c_s$ (Paak *et al.* 2013). Thus, it is reasonable to assume that there should exist a specific interaction between starting jet and flexible tube, which we do not understand clearly yet.

Therefore, in this study, we experimentally investigated the evolution of a starting jet through a circular nozzle, the flexibility of which is varied, with a focus on the relation between fluid–structure interaction and thrust generation (the hydrodynamic impulse and total circulation). The conditions of liquid flow developing through the nozzle are controlled by varying the acceleration duration (T_{acc}) and the terminal jet centreline velocity (u_t), such that the jet Reynolds number (defined as $Re_j = 2\rho_f u_t R/\mu_f$, where μ_f is the dynamic viscosity of water) and the effective acceleration time (defined as $\Pi_0 = T_{acc}u_t/L$, where L denotes the nozzle length) vary as 3290–12 500 and 1.05–2.33, respectively. To understand the phenomenon better, we simultaneously measured the deformation of the nozzle surface and flow fields (both inside and outside of the nozzle) using high-speed particle image velocimetry (PIV). Based on the analysis, we suggest the optimal condition for maximizing the thrust generation by analytically combining the shell theory and principle of conservation (of mass and momentum). Asymptotic analysis and energy balance were also used to formulate the model. We believe that the present results will significantly enhance our understanding of the fluid–structure interaction occurring in diverse flow geometries found in nature and in industry.

The remainder of this paper is organized as follows. We explain the experimental set-up and characterize the flexible nozzle used in § 2. In § 3, we discuss the effects of flexibility and flow conditions on jet evolution and the resultant thrust. In § 4, the analytical derivation of the optimal condition for maximum thrust is explained and validated. Finally, a summary and outlook of our work are given in § 5.

2. Experimental set-up and procedure

2.1. *Facility for generating a starting jet*

We established a piston–motor system to create a starting jet in a transparent acrylic chamber ($300 \times 300 \times 700$ mm^3) filled with tap water at room temperature (figure 1*a*). Actuated by a servomotor (ELDM6020, LeadShine), an aluminium piston (with a diameter of 50 mm) inside the acrylic cylinder instantly moves downward guided by a linear stage placed above the chamber. The cylindrical passage of the piston is connected to a smaller-diameter pipe (with an inner diameter of 15 mm) through a smooth contraction part (contraction ratio of 0.09). A motor driver (ELD5-400, LeadShine) and built-in control algorithm enable precise control of the motor to follow a designated velocity profile with respect to the time at the jet exit (for the rigid nozzle). We observed that there is neither mechanical vibration nor acoustic noise during the actuation, which may originate from failure in optimizing the motor–driver system.

The motor is controlled to perform impulsive acceleration of the piston (i.e. flow inside the pipe and subsequent jet flow) with time duration $T_{acc} = 0.12$–0.43 s (figure 2*a*) to reach the targeted terminal velocity, $u_t = 0.20$–0.84 m s^{-1} (figure 2*b*). Here, the acceleration time (T_{acc}) denotes the time when the jet-exit velocity at the nozzle centre (u_e) reaches 90 % of the terminal velocity ($u_e = 0.9u_t$) with the rigid nozzle. Notably, the exit velocities (u_e and u_t) are measured at $(x/D, y/D) = (0.0, -0.2)$ to avoid interference with the nozzle wall. The Reynolds number of the jet is considered to be $Re_j = 3290$–$12\,500$. As the jet flow becomes as fast as $u_t = 0.64$–0.84 m s^{-1}, it tends to weakly oscillate

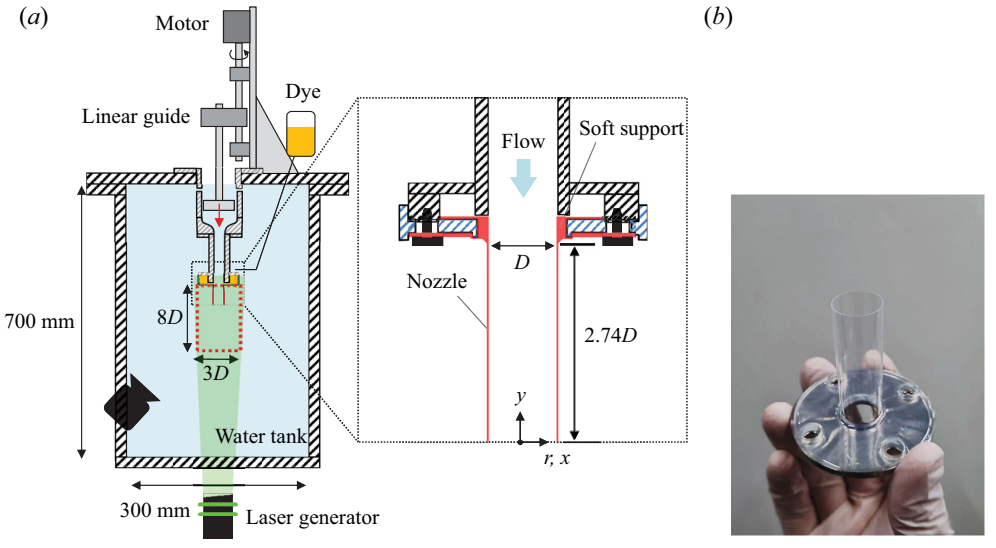

Figure 1. (*a*) Schematic diagram for the jet-flow generating facility and the detailed installation of the flexible nozzle on the piston system. (*b*) Image of the manufactured flexible nozzle with its support.

(figure 2*b*); for example, the oscillation amplitude of u_t is approximately 0.05 m s^{-1} (6.8 % of u_t) at $u_t = 0.84$ m s^{-1}. This periodic fluctuation originates from the feedback control implemented in the motor driver; however, we confirmed that the nozzle deformation is dominated by the rapid acceleration of the jet, and the slight oscillation occurring at $t > T_{acc}$ does not affect the results. Before initiating each motor operation, the piston is precisely aligned with the cylindrical container by adjusting the location of the linear guide on the uppermost plate of the chamber to avoid physical contact with the inner wall of the container. At $u_t = 0.22$ m s^{-1}, the deviation of the jet velocity at the nozzle exit is approximately $0.03u_t$. Figure 2(*c*) shows the temporal variation of the jet-velocity profile at the nozzle exit for the rigid nozzle, which shows the symmetry against the nozzle centreline. Initially, the jet flow develops with two peaks near the nozzle wall ($t/T_{acc} = 0.5$), which is attributed to the formation of a vortex ring (Didden 1979), and gradually evolves into a top-hat profile because of the boundary layer that develops inside the nozzle ($t/T_{acc} > 1.5$). Figure 2(*d*) shows the piston velocity compared with the designated and actual jet-exit velocities. Piston velocity was measured using a high-speed camera (SpeedSense M310, Dantec Dynamics), on which the oil pattern was marked to be tracked by a correlation-based algorithm. To compensate the effect of contraction geometry (see figure 1*a*), the effective piston velocity ($u_{p,eff}$) is defined based on the contraction ratio ($\simeq 0.09$), expressed as $u_{p,eff} = u_p/0.09$. We measured five sets of piston motion and their corresponding jet-exit velocities to obtain the averaged values and ensure repeatability. It is confirmed that u_e follows the planned velocity profile accurately. As shown, they have the same acceleration time (0.2 s) and target velocity (-0.2 m s^{-1}); however, there is a slight deviation between $u_{p,eff}$ and u_e in the accelerating stage. This deviation would be caused by the cylinder geometry (e.g. shape and length), piston setting (e.g. sealing and stiffness of O-ring rubber) and coefficient of motor feedback control.

Notably, the starting jet in the present study refers to the initiation of a continuous jet, indicating that the bulk velocity at the inlet of the nozzle is steady throughout the entire process, rather than a pulsed jet. In previous studies, a pulsed jet was employed to make

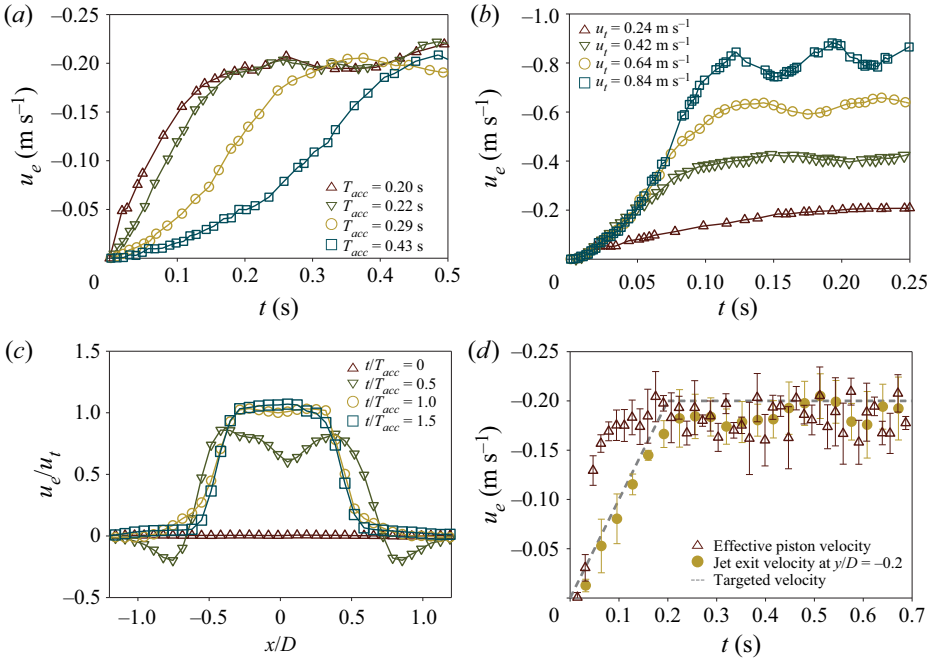

Figure 2. Time history of jet-exit velocity (u_e) with varying (*a*) acceleration time (T_{acc}) under the same terminal velocity of 0.2 m s^{-1} and (*b*) terminal velocity (u_t) with $T_{acc} = 0.12$–0.43 s. (*c*) Velocity profile in radial direction with $u_t = 0.2$ m s^{-1} and $T_{acc} = 0.2$ s. (*d*) Comparison of u_e with the piston and targeted velocities. The jet velocities were measured at $y/D = -0.2$.

all the ejected fluid slug contribute to the formation of the leading vortex ring, i.e. without the trailing jet, which was mainly characterized by the formation number (F) (Gharib *et al.* 1998; Krueger & Gharib 2003). In contrast, we are mainly interested in the role of the interplay between the flexible nozzle and the accelerating jet in thrust generation. Thus, a relatively longer jet (i.e. $F = \infty$) was chosen, which is more suitable for revealing the fundamental mechanism of the fluid–structure interaction in the jet flow.

2.2. *Preparation and installation of the flexible nozzle*

The flexible nozzle in the present study needs to satisfy two conditions: (i) it has to be thin enough to interact with the jet flow (below 200 μm for the present condition) and (ii) it must be optically accessible (i.e. transparent) to allow measurement of the fluid flow inside the nozzle. To achieve this, the dip-mould method was used to make a transparent cylindrical nozzle with a wall of thickness of $O(10$–$10^2)$ μm. First, liquid-state silicone rubber (SortaClear 40A, SmoothOn) was poured onto an acrylic cylinder rod (mould) with a diameter of 15 mm, mounted vertically on a support. The silicone flows down along the sidewall of the cylinder and gradually forms a thin film during curing. The silicone nozzle was then cut to the desired length and was carefully removed from the mould, yielding a thin-walled and transparent nozzle (figure 1*b*). By varying the mass fraction (9.1–32.4 wt%) of the thinner (Silicone Thinner, SmoothOn) to the liquid-state silicone rubber, it was possible to control the mean thickness (h) of the wall from 170 to 70 μm, and the corresponding Young's modulus (E) from 270 to 100 kPa, with a constant

Poisson's ratio of 0.4. The Young's modulus and Poisson's ratio were measured by the two-dimensional digital image correlation (DIC) technique. First, specimens of 1 mm in thickness of silicone rubber with a mass fraction of 9.1–32.4 wt% were prepared for tensile testing, on which a speckle pattern was printed using oil-based ink. Next, the tensile test machine extended the silicone rubber specimen while the high-resolution camera captured the deformed speckle pattern on the rubber surface. Based on this, a strain–stress curve is obtained, the slope of which corresponds to the Young's modulus, and the Poisson's ratio also comes out from the two-dimensional strain field calculated by digital image correlation (for details, see the supplementary material available at https://doi.org/10.1017/jfm.2022.781).

The uniformity of the thickness distribution was also verified. Along the azimuthal direction, we confirmed that the variation was negligible (a maximum deviation of 11.1 % at a mass fraction of 9.1–23.1 wt%) by measuring the cross-sections at multiple streamwise locations using a microscope. However, the nozzle wall becomes thicker at a rate of 12.5 % per nozzle diameter (= 15 mm) along the longitudinal direction, which is inevitable for the present manufacturing process. For a nozzle of 45 mm in length, the wall thickness at the nozzle tip (= 51.1 μm) is approximately 27 % thinner than that at the support (= 70 μm) for a mass fraction of 9.1 wt%. Considering this variation, the averaged thickness (h) is used as a characteristic thickness of the nozzle and, as we will discuss, the theoretical analysis (see § 4) based on the assumption of a constant wall thickness agrees well with the experimental results. On the other hand, the uncertainty in the repeatability of the manufactured nozzle is found to be within 6.6 % (in terms of the wall thickness) from six independent trials (for details, see the supplementary material available at https://doi.org/10.1017/jfm.2022.781).

In total, we tested three flexible nozzles with nozzle structural stiffnesses of $Eh = 7.0$, 14.4 and 43.2 N m^{-1}. The length (L) and inner diameter (D) of the cylinder were 41.1 and 15.0 mm, respectively, corresponding to an aspect ratio (L/D) of 2.74 (figure 1*a*). Because a higher strain rate is concentrated at the junction between the flexible nozzle and the rigid support as the nozzle is deformed by fluid forces, which can damage the silicone wall, it is necessary to mount the flexible nozzle in a robust manner. To cope with this, we manufactured a soft support together with the silicone nozzle (figure 1*a*), having a smooth strain gradient at the junction of the thin nozzle and support. In addition to flexible nozzles, we also tested a rigid nozzle as a reference, which is an aluminium tube with a wall thickness of 0.5 mm. The length and inner diameter were the same as those of the flexible nozzles. In table 1, we summarize the conditions of jet flow and the nozzle morphology considered in the present experiments.

2.3. *Measurement of flow velocity and nozzle deformation*

Considering the nominally axisymmetric nozzle geometry and resultant flow, we performed two-dimensional PIV to measure the flow fields inside and outside the nozzle. Likewise, previous studies of jet flow from a circular nozzle focused on the velocity fields measured on the centre plane (Dabiri & Gharib 2005; Gao *et al.* 2020). As tracer particles, we used glass particles (HSG-10, Dantec Dynamics) of nominal diameter of 50 μm. A 5 W Nd:YAG laser (RayPower 5000, Dantec Dynamics) generated a green-coloured laser sheet of wavelength 532 nm and illuminated the seeding particles on the measurement (x–y) plane (figure 1*a*). A high-speed camera (with a resolution of 1000 × 800 pixels) captured images of the particles with a frequency ranging from 1000 to 2000 Hz depending on the targeted jet velocity. Acquisition of the image is triggered by the

Category	Variable	Considered value(s)
Nozzle	Inner diameter (D)	15.0 mm
	Length (L)	41.1 mm
	Structural stiffness (Eh)	7.0, 14.4, 43.2, ∞ (rigid) N m^{-1}
Flow	Terminal jet velocity (u_t)	0.20–0.84 m s^{-1}
	Reynolds number (Re_j)	3290–12 500
	Acceleration time (T_{acc})	0.12–0.43 s
Dimensionless parameters	Effective acceleration time ($\Pi_0 = T_{acc}u_t/L$)	1.05–2.33
	Effective nozzle stiffness ($\Pi_1 = Eh/(\rho_f u_t^2 R)$)	1.33–120.02
	Dimensionless wave speed ($\hat{c} = (\Pi_0^2\Pi_1/2)^{1/2}$)	1.88–17.58

Table 1. Summary of the geometric and material properties of the nozzle and the jet condition considered in the present study, with the dimensionless parameters governing the starting jet–nozzle interaction.

initiation of the piston–motor system by directly hardwiring the motor driver and camera adaptor. The time delay between the motor start and image acquisition is within 1.0 μs. To capture both the development of the jet structure and the nozzle deformation, the field of view has a width of 3D (D being the inner diameter of the nozzle) and vertically ranges over 8D from the nozzle support in the jet direction.

To measure the unsteady deformation of the nozzle wall and velocity fields together, an additional image-processing step is applied to the raw images, shown in figure 3(*a*). As intended, the particles are clearly observed inside the nozzle. First, we apply a median filter to remove the particle images (figure 3*b*). In the figure, the boundary of the nozzle is detected as the position where the horizontal gradient of the grey-level intensity becomes a maximum (figure 3*c*). To enhance the detection resolution as much as the subpixel displacement (~ 0.1 pixels or 0.04 % of D), we used Gaussian interpolation. By subtracting the nozzle image from the original image, we obtained an image of particles only (figure 3*d*), which is used to measure the flow velocities. The velocity vectors were evaluated by a custom-made PIV algorithm adapting the subpixel offset-window scheme (Scarano 2001). In detail, the interrogation window (32 × 32 pixels) is offset to the subpixel displacement, pre-calculated from the larger-sized (64 × 64 pixels) interrogation window. The resultant velocity distribution has a spatial resolution of 0.066D (= 0.99 mm).

Based on error propagation analysis (Clifford 1973), the uncertainty of the flow velocity obtained by PIV can be expressed as $\delta(u_{piv}) = \sqrt{\delta(MF)^2 + \delta(\Delta s)^2 + \delta(\Delta t)^2}$ (Lawson *et al.* 1999; Choi & Park 2018; Choi, Lee & Park 2019; Maeng & Park 2021). Here, $\delta(x)$ denotes the percentage error while measuring x, MF is the pixel magnification factor, Δt is the time difference between two particle images and Δs is the displacement of the particle through Δt. In the present set-up, the percentage error involved in determining the magnification factor is measured as 0.41 % with $MF = 61.0$ μm pixel^{-1}. The error in the time interval (Δt) is estimated as 0.1 %, given that the maximum uncertainty is within 1.0 μs whereas the time interval between the image pair is 1.0 ms. Lastly, the uncertainty of Δs is calculated as 3.8 % with an average particle displacement of

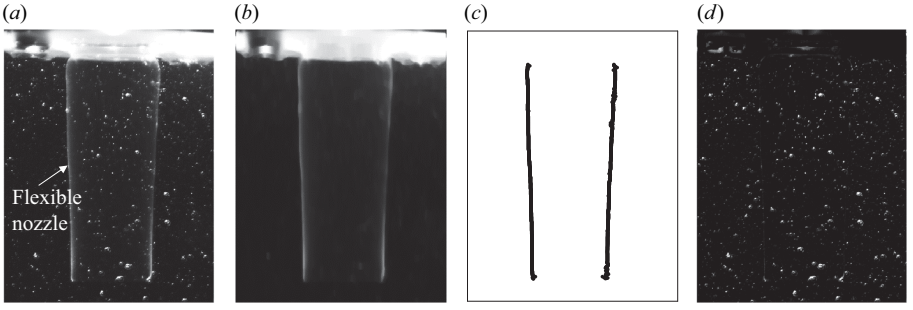

Figure 3. Image-processing procedure to measure the nozzle shape and particle image: (*a*) raw image including the image of nozzle and particles; (*b*) nozzle image; (*c*) detected nozzle shape; (*d*) image of seeding particles for PIV.

3.0 pixels (Scarano 2001). Combining all contributions, the overall uncertainty for the velocity measurement is approximately 3.8 % for the present experiments.

2.4. *Dimensionless parameters*

As we will discuss, the analysis of the fluid–structure interaction for jet flow through the deforming flexible nozzle is governed by a combination of the jet-flow conditions (terminal velocity and acceleration time) and the morphological properties of the nozzle (Young's modulus, aspect ratio and wall thickness). Here, we propose two dimensionless parameters to characterize the jet condition and the nozzle stiffness: the effective acceleration time ($\Pi_0 = T_{acc}u_t/L$) and the effective nozzle stiffness ($\Pi_1 = Eh/(\rho_f u_t^2 R)$), where R is the inner radius of the nozzle ($= D/2$). Here, Π_0 is defined as the ratio of jet acceleration time (T_{acc}) to the characteristic time scale of the starting jet (L/u_t), which is further understood as the inverse of the Strouhal number (St), $\Pi_0 = u_t T_{acc}/L = (f_{acc}L/u_t)^{-1} = St^{-1}$, by introducing $f_{acc} = 1/T_{acc}$. In previous studies of thrust generation by a flexible flapping surface, the Strouhal number was considered to explain the interaction between the geometric deformation and surrounding flow structure (Kang *et al.* 2011; Marais *et al.* 2012).

The second parameter (Π_1) is the ratio of the elastic force released during the expansion of the nozzle ($\sim EhR$; see Kraus 1967) to the inertia of the jet flow ($\sim \rho_f u_t^2 R^2$). A similar non-dimensional parameter (Π_1') was adopted in the study of the interaction between a thin flexible body and flow around it, which was derived as $\Pi_1' = E/(\rho_f u_c^2) \cdot (h/l_c)^3$ from the Euler–Bernoulli beam equation, where u_c and l_c denote the characteristic velocity and length of geometry, respectively (Shapiro 1977; Kang *et al.* 2011; Dewey *et al.* 2013; Siviglia & Toffolon 2014; Medina & Kang 2018). In those cases, the elastic body exchanges momentum with the fluid flow through the bending force ($\sim Eh^3/l_c$, if the magnitude of the beam deflection is comparable to the characteristic length) and the inertia of flow is scaled as $\rho_f u_t^2 l_c^2$. For the present problem, nozzle expansion is dominant over bending, and thus it is reasonable to consider the expansion force ($\sim EhR$) as the relevant dimensionless parameter. From the perspective of discussing the balance between elastic and fluid forces, we understand that the present parameter (Π_1) is consistent with Π_1'. In the following sections, we discuss how the behaviour of the flexible nozzle and modulation of the jet-flow structure are governed by these parameters. In § 4, their roles are emphasized by analytically showing that they appear in the governing equations describing the internal flow through the flexible nozzle and its shell deformation.

3. Experimental results and discussion

3.1. *Change in the jet characteristics with nozzle stiffness*

First, we discuss the evolution of a starting jet depending on the structural stiffness (Eh) of the nozzle (figure 4). Figure 4(*a*) shows the time history of the jet vortical structure from the rigid nozzle, for the case of $Re_j = 3286$ and $T_{acc} = 0.2$ s. As the jet starts, a pair of counter-rotating vortices representing the cross-section of the vortex ring evolves gradually (numbered as '1' in figure 4*a-ii*), which pinches off from the nozzle exit (figure 4*a-iii*) at $t/T_{acc} \simeq 0.76$. Following the primary vortex, a trailing shear layer develops and rolls up into the secondary vortex ring (numbered as '2' in figure 4*a-iv*). As the flow develops, the lateral distance between counter-rotating vortices, i.e. size of the vortex ring, increases, and the secondary vortex is entrained and merged into the primary vortex (figure 4*a-v*,*a-vi*), whereas the third and fourth vortices (numbered as '3' and '4' in the figure) show up successively along with the jet shear layer. Overall, this temporal evolution of the vortical structure of the starting jet from a circular nozzle is consistent with that observed in a previous study (Zhao, Frankel & Mongeau 2000).

Under the same flow conditions, the change in the jet vortical structures from flexible nozzles with different structural stiffness ($Eh = 43.2$, 14.4 and 7.0 N m^{-1}) is shown in figure 4(*b–d*), together with the nozzle profile. With flexible nozzles, similar flow structures are retained such that the primary vortex develops (figure 4*b-ii–d-ii*) and pinches off (figure 4*b-iii–d-iii*) as the jet flow accelerates. However, the pinch-off instant of the primary vortex from the shear layer is affected by the flexibility of the nozzle. It occurs at $t/T_{acc} = 0.35$, 0.6 and 0.77 for $Eh = 43.2$, 14.4 and 7.0 N m^{-1}, respectively, while it is at $t/T_{acc} = 0.76$ for the rigid nozzle ($Eh = \infty$). Thus, it is understood that the promotion and delay of the vortex pinch-off for the relatively stiffer ($Eh = 43.2$ and 14.4 N m^{-1}) and softer ($Eh = 7.0$ N m^{-1}) nozzles, respectively, are closely associated with the expansion and contraction behaviour of the deformable nozzle, which is discussed in the following sections. Away from the nozzle exit, the primary vortex merges with the secondary vortex (figure 4*b-v–d-v*) while moving downward. For $Eh = 43.2$ N m^{-1}, interestingly, the merging of the first and second vortex rings is less organized than that in other cases, which is judged from the scattered small-scale eddies around the merged vortex (figure 4*b-vi*). In addition, the radius of the merged vortex ring ($\sim 0.9D$) is larger than others ($\sim 0.8D$). This is related to the early pinch-off ($t/T_{acc} \simeq 0.35$) of the primary vortex; the strength of the secondary vortex ring is comparable (figure 4*b-iv*) with the primary vortex ring with an insufficient feeding of the vorticity from the shear layer. This results in a more vigorous interaction between the vortex rings, which does not occur for other nozzles (figure 4*a-iv*,*c-iv*,*d-iv*). After merging with the secondary vortex ring, the primary vortex is convected downward faster as the nozzle becomes more flexible, indicated by the longer distance travelled from the nozzle exit: at $t/T_{acc} = 2.66$, it is measured to be $3.7D$ ($Eh = 43.2$ N m^{-1}), $4.5D$ (14.4 N m^{-1}) and $5.0D$ (7.0 N m^{-1}) (figure 4*b-vi–d-vi*). The convection speed of the vortex is proportional to its circulation (Γ_{vor}), the growth rate of which is associated with the jet-exit velocity (u_e), expressed as $\mathrm{d}\Gamma_{vor}/\mathrm{d}t = u_e^2/2$, if the horizontal velocity is absent at the jet exit (Saffman 1995; Krieg & Mohseni 2013). For the present set-up, the pinch-off time and the jet-exit velocity increase (see figure 7*b*) with decreasing Eh, which results in faster migration of the vortex ring.

Because the amplitude of nozzle deformation is less than 5 % of the nozzle diameter, which is not sufficiently large to make a quantitative analysis (figure 4), we additionally performed subpixel image processing (Scarano 2001) to extract the unsteady variation of radial displacement (w_n) of the nozzle wall from processed images (figure 2*c*) with

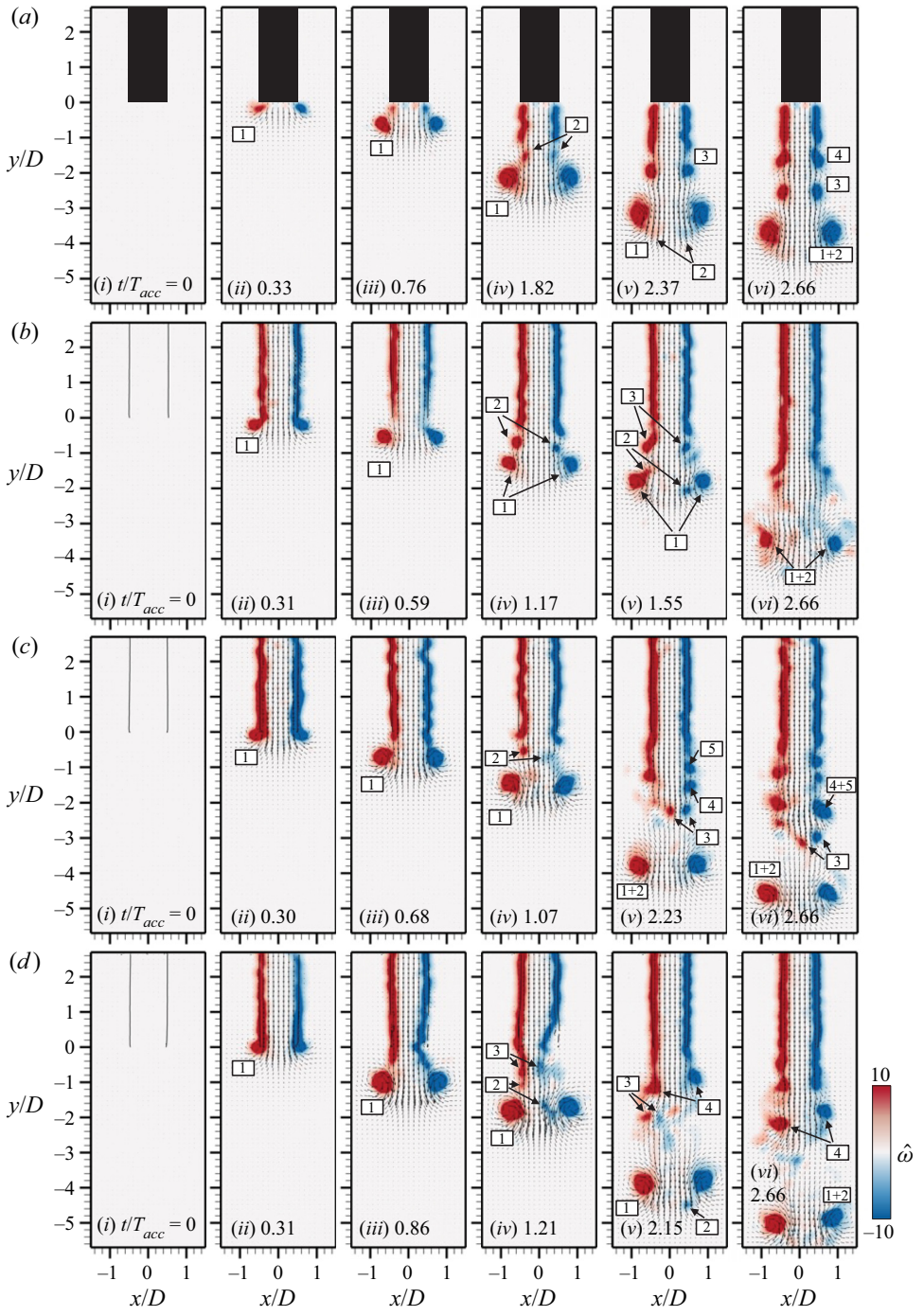

Figure 4. Evolution of jet flow (velocity vectors and vorticity ($\hat{\omega} = \omega D/u_t$) contour) depending on the structural stiffness (Eh) of the nozzle at $Re_j = 3286$ and $T_{acc} = 0.2$ s: (*a*) $Eh = \infty$ ($\Pi_0 = 1.05$ and $\Pi_1 = \infty$); (*b*) 43.2 N m^{-1} (1.05 and 120.02); (*c*) 14.4 N m^{-1} (1.05 and 40.0); (*d*) 7.0 N m^{-1} (1.05 and 19.45). The profile of the deformed nozzle is drawn as black lines, and the numbered index in each box indicates the birth order of each vortex.

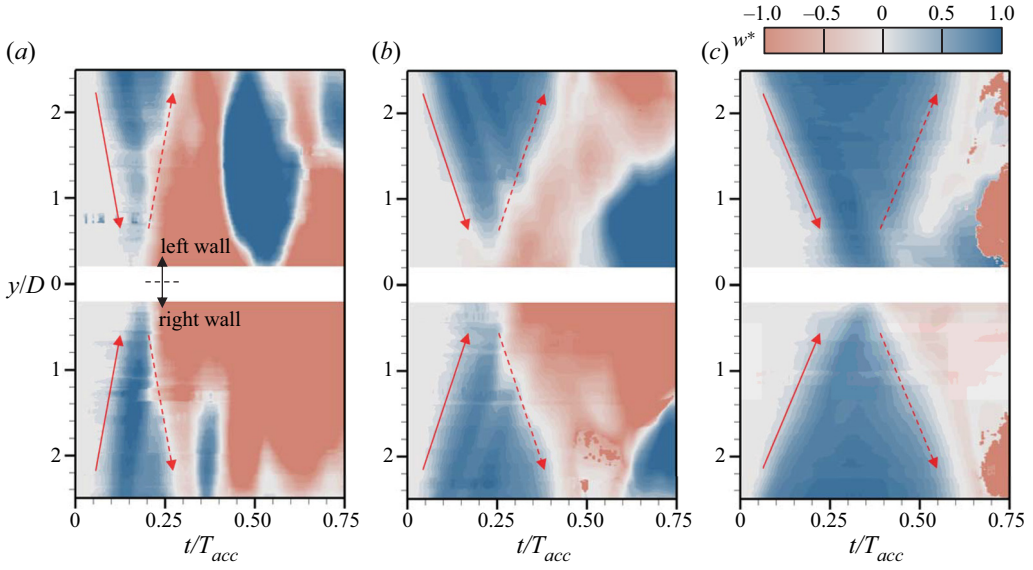

Figure 5. Spatio-temporal contour of the normalized nozzle displacement ($\hat{w}^* = w_n/w_{n,max}$) at $Re_j = 3286$ and $T_{acc} = 0.2$ s, depending on the structural stiffness: (*a*) $Eh = 43.2$; (*b*) 14.4; (*c*) 7.0 N m^{-1}. Here, the maximum displacement $w_{n,max}/D$ is measured as (*a*) 0.010, (*b*) 0.022 and (*c*) 0.036.

a resolution of approximately $0.0004D$. The measured $w_n(y, t)$ is further normalized with the maximum radial displacement ($w_{n,max}$) as $w_n^* = w_n/w_{n,max}$. Note that the nozzle deformation was not averaged circumferentially but was measured on one centre plane considering the axisymmetric expansion and contraction of the nozzle. Figure 5 shows the spatio-temporal contour of w_n^* with varying Eh of the nozzle for the same flow conditions as those of figure 4. As shown, the nozzle initially expands axisymmetrically and reaches the maximum expansion, which is delayed with decreasing Eh: $w_{n,max} = 0.0040D$ (at $t/T_{acc} = 0.15$), $0.012D$ (at 0.20) and $0.024D$ (at 0.35) for $Eh = 43.2$, 14.4 and 7.0 N m^{-1}, respectively. Once the expansion wave is transmitted to the nozzle exit ($y/D = 0$), it returns to the original position with almost the same speed (note that the slopes of the solid and dashed lines drawn around the first expansion wave are equivalent). That is, the nozzle contracts towards its original shape ($w_n = 0$) without a delay. After one cyclic transmission of the expansion wave, the nozzle subsequently undergoes irregular collapses (buckling that causes flow asymmetry inside the nozzle in figure 4*d-iv*) because of the negative pressure inside the nozzle induced by the accelerated fluid jetting out of the nozzle (at $t/T_{acc} > 0.25$, 0.4 and 0.60 for $Eh = 43.2$, 14.4 and 7.0 N m^{-1}, respectively) (figure 5). At this stage, optical edge detection shows its limitation as the nozzle wall is folded and wrinkled, over-reflecting light, and we removed the corresponding data in figure 5 to avoid any misunderstanding. Notably, the jet characteristics responsible for thrust generation are mainly relevant to the stage of expansion–contraction by the first surface wave (i.e. $t/T_{acc} < 0.25$, 0.4 and 0.60 for $Eh = 43.2$, 14.4 and 7.0 N m^{-1}, respectively). Thus, in the following sections, we focus on the initial stage to discuss the optimal fluid–structure interaction condition to achieve enhanced thrust generation.

As highlighted with arrows in figure 5, expansion–contraction of the nozzle results in the surface wave propagating with constant speed (the edge of displacement contour is fitted linearly) between the nozzle support ($y/D \simeq 2.5$) and tip ($y/D = 0$). Through this surface

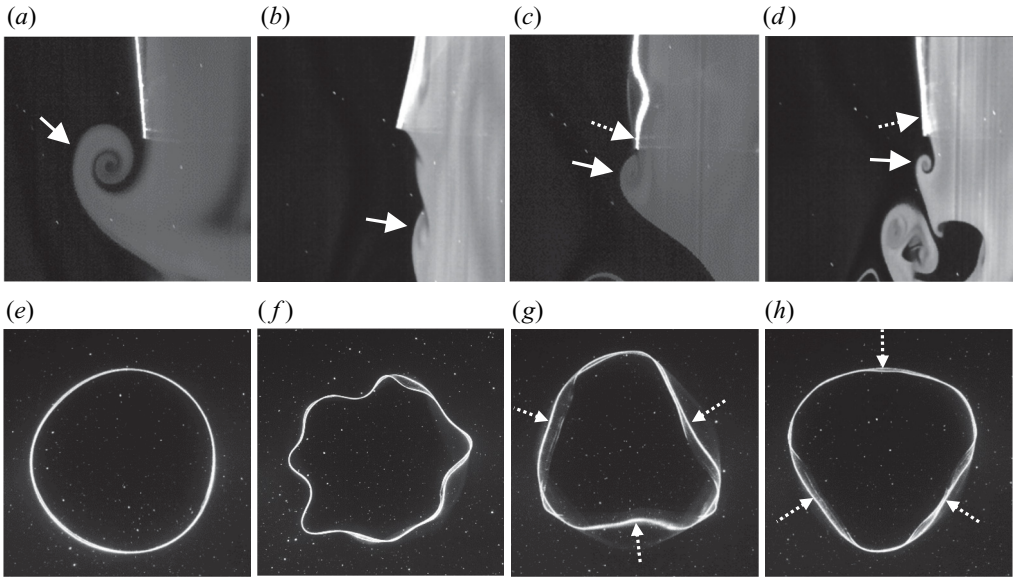

Figure 6. (*a–d*) Temporal variation of dye visualization of vortex formation for the case of $Eh = 7.0$ N m^{-1} and (*e–h*) the deformation of the nozzle tip viewed from the bottom at the same instant: (*a*,*e*) $t/T_{acc} = 0.7$; (*b*,*f*) 1.7; (*c*,*g*) 2.5; (*d*,*h*) 2.8. The flow conditions are $Re_j = 3286$ and $T_{acc} = 0.2$ s. In (*e–h*) the laser sheet is positioned at $y/D = 0.1$ to highlight the profile of the nozzle tip.

deformation, the elastic energy stored during expansion is transported to the ejecting jet, increasing the impulse of the jet flow. The first cycle (T_c) of expansion–contraction gets longer as the nozzle becomes more flexible; for example, $T_c/T_{acc} = 0.3$, 0.4 and 0.6 for $Eh = 43.2$, 14.4 and 7.0 N m^{-1}, respectively. Interestingly, this matches the instant when the primary vortex ring pinches off: $0.35T_{acc}$, $0.6T_{acc}$ and $0.77T_{acc}$ (for $Eh = 43.2$, 14.4 and 7.0 N m^{-1}, respectively), indicating the close relationship between nozzle deformation and vortex evolution, which is further analysed in the following sections.

The visualization shown in figure 6 describes the mechanism of vortex formation (figure 6*a–d*) and nozzle deformation along the azimuthal direction (figure 6*e–h*) for the case of $Eh = 7.0$ N m^{-1} corresponding to the most flexible condition tested. Near the end of jet acceleration ($t/T_{acc} = 0.7$), the primary vortex is developing at the nozzle exit (figure 6*a*), which subsequently pinches off from the shear layer and convects downstream. At this time, the nozzle tip maintains its circular shape (figure 6*e*). After acceleration of the jet is completed ($t/T_{acc} = 1.7$), the jet shear layer following the primary vortex becomes unstable (indicated by the arrow in figure 6*b*), which rolls up into the secondary vortex. As can be expected from figure 4, the nozzle tip deforms (shrinks) beyond its original size, driven by the strong jet inertia, resulting in a wrinkled structure (figure 6*f*), which is known to have lower energy compared with the axisymmetric shape under the same pressure distribution (Hibbeler 2013). For a flexible nozzle, the roll-up and formation of subsequent (third, fourth and so on) vortex rings occur at the nozzle tip (figure 4*b-v–d-v*) driven by its lateral flapping movement, rather than the growth of the shear-layer instability, which is the leading cause in the jet from the rigid nozzle (figure 4*a-vi*). Figures 6(*c*) and 6(*d*) show the formation of the third and fourth vortices triggered by the movement of the nozzle tip (noted with the solid and dotted arrows, respectively, in the figures). During this process,

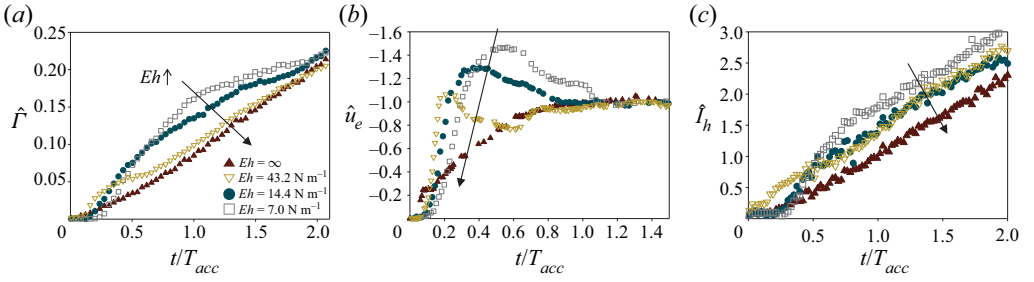

Figure 7. Temporal evolution of the jet-flow characteristics: (*a*) dimensionless total circulation, $\hat{\Gamma} = \Gamma/(u_t D)$; (*b*) dimensionless jet-exit velocity, $\hat{u}_e = u_e/u_t$; (*c*) relative hydrodynamic impulse, $\hat{I}_h = I_h/I_{h,rigid}|_{t/T_{acc}=1.0}$. For the cases plotted, $Re_j = 3286$ and $T_{acc} = 0.2$ s. The solid arrow in each panel denotes the direction of increasing Eh.

flapping motion of the nozzle tip results in a triangular shape, the orientation of which is synchronized with sequential vortex shedding (figure 6*g*,*h*). Interestingly, the nozzle deforms in an organized shape after the transient (shedding of the second vortex ring) stage of irregular wobbling. For the case of $Eh = 7.0$ N m^{-1}, the wavenumber (i.e. the number of waves on the circumference) along the circumferential direction corresponding to this organized deformation is 3.0 (triangle), and it varies depending on the stiffness of the nozzle and the jet conditions. Although this is not the primary concern of the present study and requires a detailed structural analysis in the future, we performed a brief modal analysis to understand this behaviour (see Appendix A).

On the other hand, the inherent azimuthal instability of a vortex ring (Widnall & Sullivan 1973; Widnall, Bliss & Tsai 1974; Hattori & Fukumoto 2003; Fukumoto & Hattori 2005; Dazin, Dupont & Stanislas 2006) can be a potential cause of the circumferential deformation of the nozzle. This instability originates from the resonance between azimuthal perturbations with two different wavenumbers and simultaneously amplifies the disturbance in a linearly developing stage. It was reported that the growth of azimuthal instability in a vortex ring incurs a marked decrease in both the circulation and translational velocity of a vortex ring because of the generation of secondary vortex and subsequent nonlinear processes (Dazin *et al.* 2006; Bergdorf, Koumoutsakos & Leonard 2007). However, as we discuss below (see figure 8), the vortex ring tends to grow by being fed continuously from a shear layer or merging with following vortices. Therefore, the waviness of the nozzle tip (figure 6*f*) seems to be irrelevant to the instability of a vortex ring; rather, it is related to the fluid–structure interaction of the elastic nozzle. On the other hand, the present flexible nozzle can be stretched (figure 6*a*,*e*) or bent (figure 6*b–d*,*f*,*g*). Through stretching, the nozzle stores and releases elastic energy to the jet flow until the expansion–contraction cycle ends (figures 5 and 8). Bending occurs after this stage (figure 6*f–h*); however, the increment to the hydrodynamic impulse is found to be negligible. As we discuss in relation to figure 7(*c*), bending does not produce additional thrust but contributes to the generation of successive vortex rings (figure 6*c*,*d*).

Das *et al.* (2018) reported that a flexible flap installed at the outlet of a slit (plane) nozzle is deformed by a starting jet approximately twice the nozzle diameter ($\sim 2D$) under similar conditions ($Re_j = 2700$, $T_{acc} = 0.1$ s, $D = 15$ mm and $L/D = 3$), which is larger than that in the current study ($< 0.2D$). For the two-dimensional flap, the fluid pressure inside the nozzle due to jet acceleration balances with the bending moment rather than the tensile force, while the latter dominates in the flow through the circular

flexible nozzle. A brief scale analysis is given as follows. When the amplitude of nozzle deflection is δ_b, the bending force can be scaled as $Eh^3\delta_b/l_c^2$ (Shapiro 1977; Kang *et al.* 2011; Dewey *et al.* 2013; Siviglia & Toffolon 2014; Medina & Kang 2018), whereas the tensile force is associated with $Eh\delta_t$, where δ_t denotes the displacement of the axisymmetric expansion (Kraus 1967). If the nozzle is very thin (i.e. $h/l_c \ll 1.0$), $\delta_b/\delta_t \sim (l_c/h)^2 \gg 1.0$, indicating that the bending amplitude is much greater than that by expansion.

Figure 7(*a*) shows the temporal variation of the total circulation (Γ) depending on nozzle stiffness, which is calculated as $\Gamma = 0.5\int_C |\omega_\theta|\,\mathrm{d}A$, where the integration area C ranges between $-2 \le x/D \le 2$ and $-5.5 \le y/D \le 0$ on the measurement plane, excluding the area inside the nozzle located at $y/D > 0$. It is further non-dimensionalized as $\hat{\Gamma} = \Gamma/(u_t D)$. Consistent with the jet-flow development in figure 4, the total circulation at $t/T_{acc} = 1.0$ (when the acceleration ends) is maximum for the case of $Eh = 7.0$ N m^{-1}, and it decreases with increasing Eh. When we consider the trends closely, an initial time lag (up to $0.2T_{acc}$) is observed before $\hat{\Gamma}$ starts to rapidly increase, which is attributed to the time required for the fluid to be accumulated inside the nozzle sufficiently to radially expand the nozzle. The fluid is then released during the contraction phase through the nozzle exit, which increases the circulation (during $t/T_{acc} \simeq 0.2$–1.0). As the nozzle becomes more flexible (smaller Eh), $\hat{\Gamma}$ increases sharply for a longer duration because the contraction (as well as the expansion) time of the nozzle is increased, as shown in figure 5. While recovering the original shape ($t/T_{acc} > 1.0$), the growth rate of the total circulation is reduced, which gradually converges to that for the rigid nozzle. This can be understood from the conservation of the circulation according to the Helmholtz theorem. Because all nozzles are supplied with the same influx of vorticity through the same movement of the piston–motor system, the time history of the total circulation contained in the control volume has to be identical. After jet acceleration ends and the nozzle recovers its original shape, the influx from different nozzles becomes identical and the total circulation converges.

Figure 7(*b*) shows the jet velocity at the nozzle exit normalized by the terminal jet velocity, $\hat{u}_e = u_e/u_t$. As the flow inside the flexible nozzle is accelerated, $\hat{u}_e$ abruptly increases after a short time lag owing to nozzle expansion and reaches the maximum velocity faster than the terminal velocity (u_t), i.e. $|\hat{u}_e| \ge 1.0$. Clearly, the maximum jet-exit velocity becomes higher as the nozzle becomes more flexible, which is responsible for the rapid increase of Γ (figure 7*a*). The time (t_{max}) at which the jet reaches the maximum velocity is delayed as the nozzle becomes flexible; it is $t_{max}/T_{acc} = 0.2$, 0.3 and 0.6 for $Eh = 43.2$, 14.4 and 7.0 N m^{-1}, respectively. It coincides with the instants at which the nozzle contraction ends (figure 5) and the vortex ring pinches off (figure 4), indicating that the fluid–structure interaction associated with nozzle deformation governs the jet characteristics. It is meaningful to mention that the agility of the nozzle system as well as the thrust (i.e. the maximum velocity) are markedly enhanced using the flexible surface. For a flexible nozzle of $Eh = 43.2$ N m^{-1}, for example, only $0.17T_{acc}$ is required to reach 90 % of terminal velocity. This implies that the elastic appendage can increase the accelerating performance of the system. In physiology and biomimetic engineering, a flexible actuator quickly releases the stored force in movements such as jumping, capturing prey and escaping, and it is even advantageous in overcoming physiological and neurological limits (Higham & Irschick 2013; Haldane *et al.* 2016).

To quantify the effect of nozzle flexibility, the hydrodynamic impulse (I_h) is calculated, which has been used as a measure of thrust generation (Krueger & Gharib 2003). It is

expressed as follows (Saffman 1995):

$$I_h = \frac{1}{2}\rho_f \int_C \boldsymbol{x} \times \boldsymbol{\omega}\, \mathrm{d}V. \tag{3.1}$$

Here, $\boldsymbol{x} = (r, \theta, y)$ is the position vector whose origin is located at the centre of the nozzle exit (figure 1*b*) and the vorticity vector is given as $\boldsymbol{\omega} = (\omega_r, \omega_\theta, \omega_y)$. Considering that the flow is axisymmetric ($\omega_r = \omega_y = 0$) and $\mathrm{d}V = 2\pi r\, \mathrm{d}A$, hydrodynamic impulse can be calculated as $I_h = 0.5\pi\rho_f \int_C r^2 |\omega_\theta(r, y)|\, \mathrm{d}A$, where the control surface C is the same as for the calculation of Γ (figure 7*a*) and ω_θ denotes the component of vorticity perpendicular to the measurement plane. In figure 7(*c*), we compare the hydrodynamic impulse from the flexible nozzle with that from the rigid nozzle, which is defined as $\hat{I}_h = I_h/I_{h,rigid}|_{t/T_{acc}=1.0}$. As expected, the relative hydrodynamic impulse becomes stronger as the nozzle becomes more flexible. When the jet acceleration ends ($t/T_{acc} = 1.0$), $\hat{I}_h$ becomes 1.44 (for $Eh = 43.2$ N m^{-1}), 1.46 (14.4) and 1.9 (7.0). Thus, the flexible nozzle with $Eh = 7.0$ N m^{-1} (the most flexible case among those considered) can produce a thrust 90 % larger than that produced by the rigid nozzle instantly.

Considering the potential application of a flexible nozzle in a jet-propelled robot, we estimated the hydrodynamic impulses (I_h) in figure 7(*c*) in a physical unit, which is $I_h = 0.93$, 1.25, 1.39 and 1.79 mN s at $t/T_{acc} = 1$ for $Eh = \infty$, 43.2, 14.4 and 7.0 N m^{-1}, respectively. Krueger & Gharib (2003) reported an impulse of a starting jet of around 6.0–6.6 mN s, when $F = 3.0$ (for the present study, the instantaneous formation number (F_i) defined by Limbourg & Nedić (2021*a*) is calculated as $F_i = 2.7$ at $t/T_{acc} = 1$). Since the contribution of the pressure to the impulse is less than 10 % of the total impulse (Gao *et al.* 2020), the total impulse can be roughly estimated by the momentum contribution ($\sim \rho_f u_e^2 A$, where u_e and A denote the velocity and cross-section at the nozzle exit, respectively). By comparing the jet velocity and the exit area, it is estimated that the jet impulse from Krueger & Gharib (2003) would be 4.5 times larger than ours, which is consistent with the measurement.

As we have shown, the increase in the jet impulse is associated with delayed vortex pinch-off, and previous studies tried to achieve this by controlling the exit diameter of the nozzle (Dabiri & Gharib 2005) and by inducing a radial velocity of the jet using the converging circular nozzle (Krieg & Mohseni 2013), by which the jet thrust was enhanced by 35 % and 70 %–75 %, respectively. In the present study, compared with active control (Dabiri & Gharib 2005) requiring external energy input, the hydrodynamic impulse is improved by a passive fluid–structure interaction, and the magnitude of the increment is larger. On the other hand, the increment of the impulse may be contributed by either an increase in the fluid momentum (i.e. the accelerated jet exit velocity) or a pressure rise at the exit, which is attributed to the radial velocity at the exit (Krieg & Mohseni 2013). Because the radial component of the velocity is negligible compared with the streamwise one in the present configuration, the augmentation of the jet impulse is caused by the increased fluid momentum (evidenced in figure 7*b*), and it is closely related to the expansion–contraction of the nozzle (an analytical analysis of this is given in § 4).

As shown in figure 4, on the other hand, the evolution of a leading vortex ring from the nozzles is also affected by nozzle flexibility. To investigate this, the horizontal (x_v) and vertical (y_v) locations of vortex ring are detected based on the maximum vorticity (ω_{max}). Then, its translational velocity (V_v) is calculated as $V_v = \mathrm{d}y_v/\mathrm{d}t$, and the vortex radius (R_v) is obtained from x_v. Finally, the core radius (a_v) of a vortex ring is defined as the equivalent radius of the closed loop at which the vorticity corresponds to $0.9\omega_{max}$ (Das, Bansal & Manghnani 2017). Das *et al.* (2017) showed that the core radius obtained

based on vorticity is comparable with the velocity-based one (Arakeri *et al.* 2004) as well as the theoretical prediction of $a_v = \sqrt{4\nu T_s}$ (where T_s is the stroke time during vortex ring generation), which assumes that the vorticity in a core follows a Gaussian distribution (Saffman 1995). To measure the circulation of vortex ring (Γ_v), the inner region of a vortex on the two-dimensional flow field should be specified, on which the vorticity is integrated. We used the swirling strength (λ) to define that region with a closed curve (Zhang & Rival 2020). That is, based on the maximum swirling strength (centre of the vortex ring), the isocurve of $0.1\lambda_{max}$ is drawn and the vorticity is integrated to obtain Γ_v. Considering the symmetric vortex ring, the variables mentioned above were obtained for both sides ($x > 0$ and $x < 0$) and averaged, which were normalized with the nozzle diameter (D) and jet terminal velocity (u_t).

Figure 8 shows the temporal variation of the characteristics of a leading vortex ring depending on Eh. Figure 8(a) shows that the vortex ring from a flexible nozzle rapidly accelerates and saturates (at $t/T_{acc} = 0.5$–1.0) to a specific velocity that increases with decreasing Eh, whereas the vortex from the rigid nozzle gradually accelerates. At $t/T_{acc} > 2.0$, vortex velocity slightly decreases for flexible nozzles of $Eh = 14.4$ and 7.0 N m^{-1}, while that from the stiffer nozzle ($Eh = 43.2$ N m^{-1}) marginally increases at $t/T_{acc} \simeq 1.5$. The trend of circulation (figure 8b) is similar to that of V_v. However, the circulation tends to remain constant for $Eh = 14.4$ and 7.0 N m^{-1}, and slightly increases for $Eh = 7.0$ N m^{-1}. Assuming that the vortex radius (R_v) is much larger than core radius (a_v), and the vorticity follows the Gaussian distribution inside a core, translational velocity (V_v) of a vortex ring is expressed as $V_v = \Gamma_v/4\pi R_v(\ln(8R_v/a_v) - 0.552)$ (Lamb 1945; Saffman 1970; Sullivan *et al.* 2008). This relation explains the similarity between the translational velocity (figure 8a) and circulation (figure 8b) of a vortex ring because R_v and a_v are quite similar for all nozzles (figure 8c,d). Interestingly, the difference in both radii is barely noticeable between nozzles despite the strong nozzle–jet interaction (figure 6), except for R_v of $Eh = 43.2$ N m^{-1}. In the present configuration, the piston supplies momentum for entire duration of measurement (thus, the stroke time is the same for all cases), and the vorticity is sufficiently fed to vortex ring for all nozzles. Therefore, considering the theoretical model of Saffman (1995), the core radius is almost the same for all nozzles (figure 8c). Meanwhile, for $Eh = 43.2$ N m^{-1}, the vortex radius becomes larger than others at $t/T_{acc} > 1$. This is attributed to the vortex interaction, shown in figure 4b-iv; that is, the early pinch-off of a leading vortex results in coalescence (at $t/T_{acc} \simeq 1.5$) with subsequent vortices, enlarging the vortex radius of the leading vortex ring, and also slightly increasing the translational velocity (figure 8a) and circulation (figure 8b). Vortex merging also happens for $Eh = 14.4$ (figure 4c-v) and 7.0 (figure 4d-v,vi) but circulation and radius are not affected, unlike the case of $Eh = 43.2$ N m^{-1}. This is because the trailing vortex ring is not sufficiently large to incur the vortex interaction but is passively entrained by the leading vortex. In brief, the nozzle flexibility alters the jet vortices not only for the generation and growth of a leading vortex but also for the birth of trailing vortices (figure 6c,d,g,h).

3.2. *Effect of flow condition on jet characteristics*

Figure 9 shows the temporal evolution of the jet characteristics when Re_j increases to 12 555 and T_{acc} is shortened to 0.12 s ($\Pi_0 = 2.33$ and $\Pi_1 = 1.33$–8.22). For the cases shown in figure 7, $Re_j = 3286$ and the acceleration time is 0.2 s, corresponding to $\Pi_0 = 1.05$ and $\Pi_1 = 19.45$–120.02. Interestingly, the total circulation for the intermediate flexibility ($Eh = 14.4$ N m^{-1}) is larger than that for the more flexible nozzle

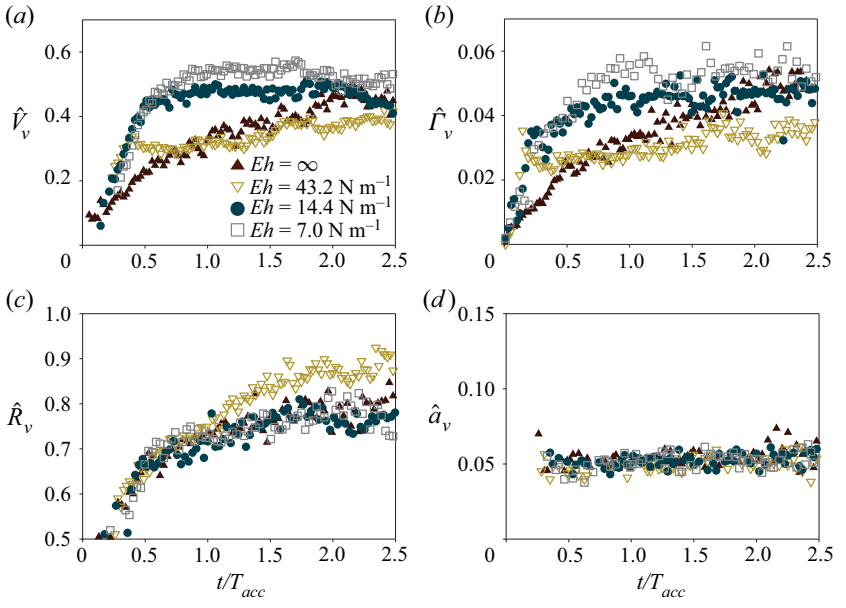

Figure 8. Temporal variation of the characteristics of a leading vortex ring depending on Eh: (a) translational velocity of the vortex ($\hat{V}_v = V_v/u_t$); (b) vortex circulation ($\hat{\Gamma}_v = \Gamma_v/(u_t D)$); ($c$) vortex radius ($\hat{R}_v = R_v/D$); ($d$) core radius ($\hat{a}_v = a_v/D$). For the cases plotted, $Re_j = 12\,555$ and $T_{acc} = 0.12$ s.

($Eh = 7.0$ N m^{-1}) at $t/T_{acc} = 1.0$ (figure 9a), contrary to the result in figure 7(a), in which the maximum total circulation (at $t/T_{acc} = 1.0$) is achieved with the minimum stiffness ($Eh = 7.0$ N m^{-1}). Similarly, reversed trends in the jet exit velocity (figure 9b) and hydrodynamic impulse (figure 9c) are observed. The maximum $\hat{u}_e$ and $\hat{I}_h$ achieved with $Eh = 14.4$ N m^{-1} at $t/T_{acc} = 1.0$ are slightly larger than those for $Eh = 7.0$ N m^{-1}. This implies that enhanced flexibility does not always augment the jet thrust, whereas many previous studies tended to conclude that the aerodynamic (or hydrodynamic) performance of a body is enhanced monotonically as its surface becomes more flexible (Kim & Gharib 2011; Marais *et al.* 2012; Das *et al.* 2018). Rather, there should be an optimal flexibility for maximizing the thrust, and it is not only determined by the stiffness but also depends on the flow condition (such as the acceleration time and the terminal velocity for the present problem). Meanwhile, the optimal condition for enhancing thrust (or efficiency) of a flexible flapping wing (panel) is closely associated with the phase lag in the angular displacements of the root and the deflected tip (Kang *et al.* 2011; Dewey *et al.* 2013; Quinn *et al.* 2014; Park *et al.* 2016). The physical significance of the phase lag implies that the time-scale ratio of the structural natural frequency to the undulation (flapping) frequency governs thrust generation and vortical structures emanating from the flexible body. Similarly, for the present flexible nozzle, we need a similar approach or a parameter that can compare the jet-flow time scale with the structural response time scale (material and geometrical properties of the nozzle).

In figure 10, we show the temporal variation of the averaged nozzle displacement along the radial direction, defined as $w^*_{avg} = (w^*_{left} + w^*_{right})/2$, where w^*_{left} and w^*_{right} correspond to the normalized radial displacement at $x < 0$ and $x > 0$, respectively. The operation condition is the same as that for figure 9. Note that the contour range is deliberately biased to positive value to effectively show the expansion–contraction behaviour of the nozzle.

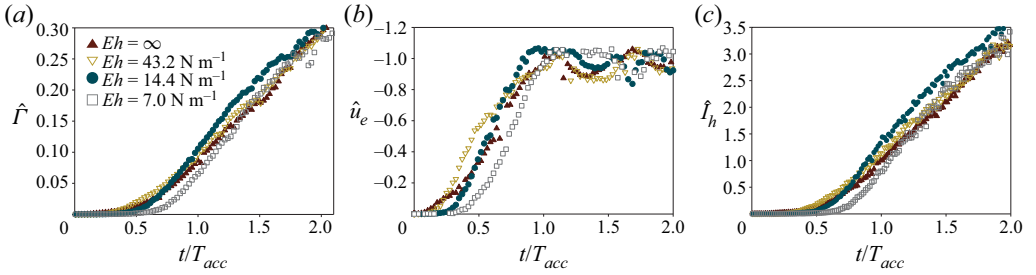

Figure 9. Temporal evolution of jet-flow characteristics: (*a*) dimensionless total circulation, $\hat{\Gamma} = \Gamma/(u_t D)$; (*b*) dimensionless jet-exit velocity, $\hat{u}_e = u_e/u_t$; (*c*) relative hydrodynamic impulse, $\hat{I}_h = I_h/I_{h,rigid}|_{t/T_{acc}=1.0}$. For the cases plotted, $Re_j = 12\,555$ and $T_{acc} = 0.12$ s.

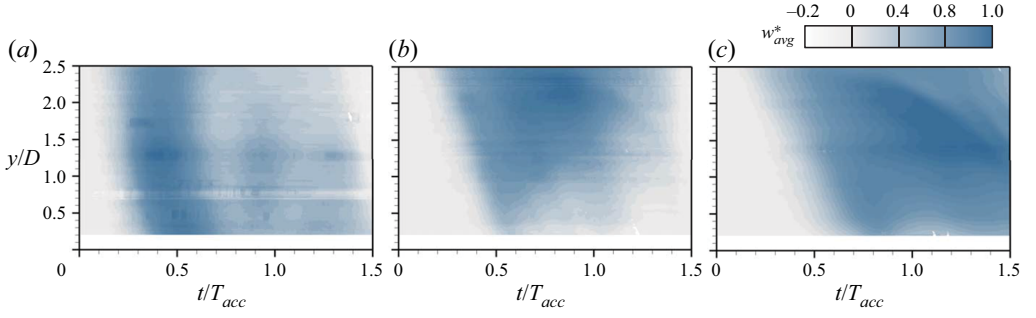

Figure 10. Spatio-temporal contour of the averaged nozzle displacement ($w^*_{avg} = (w^*_{left} + w^*_{right})/2$) at $Re_j = 12\,555$ and $T_{acc} = 0.12$ s, depending on the structural stiffness: (*a*) $Eh = 43.2$; (*b*) 14.4; (*c*) 7.0 N m^{-1}. Here, the maximum displacement, $w_{n,max}/D$, is given as (*a*) 0.025, (*b*) 0.062 and (*c*) 0.14.

Similar to the case of lower $Re_j = 3285$ (figure 5), the flexible nozzle radially expands and contracts as the jet accelerates, and the period of expansion–contraction (t_{cycle}) becomes longer as the stiffness of the nozzle decreases. For the stiffest case ($Eh = 43.2$ N m^{-1}), nozzle contraction is completed at $\sim 0.6T_{acc}$ when the growth rate of the exit velocity is significantly reduced (figure 9*b*), which is attributed to the early end of the supply of elastic energy from the nozzle to the jet flow. Notably, for $Eh = 14.4$ N m^{-1}, the expansion–contraction cycle corresponds to the time for jet acceleration ($t_{cycle} \simeq 1.4T_{acc}$), indicating that elastic energy stored in the nozzle is fully transferred to the flow during acceleration. For a nozzle with $Eh = 7.0$ N m^{-1}, contraction persists up to $t/T_{acc} > 1.5$, implying that the elastic energy does not entirely add fluid momentum even after jet acceleration ends. That is, the response of the nozzle lags behind the acceleration of the jet.

Based on our analyses so far, the expansion–contraction cycle (t_{cycle}) should be comparable to the acceleration time of the jet, $t_{cycle} \simeq T_{acc}$, to enhance thrust generation. Precisely, on the other hand, the nozzle may further release energy at $t > t_{cycle}$ until the nozzle fully contracts at $t = t_{fc}$. Therefore, the effective time required to maximize thrust generation must cover the duration for complete nozzle shrinkage (t_{fc}). Based on the present measurements (figure 5*a*,*b*), the time span of $t_{cycle} < t < t_{fc}$ is comparable to half of the expansion–contraction cycle; thus, the optimal jet acceleration time (T_{acc}) should match $t_{fc} \simeq 1.5t_{cycle}$. Hence, it is expected that the elastic energy stored in the flexible

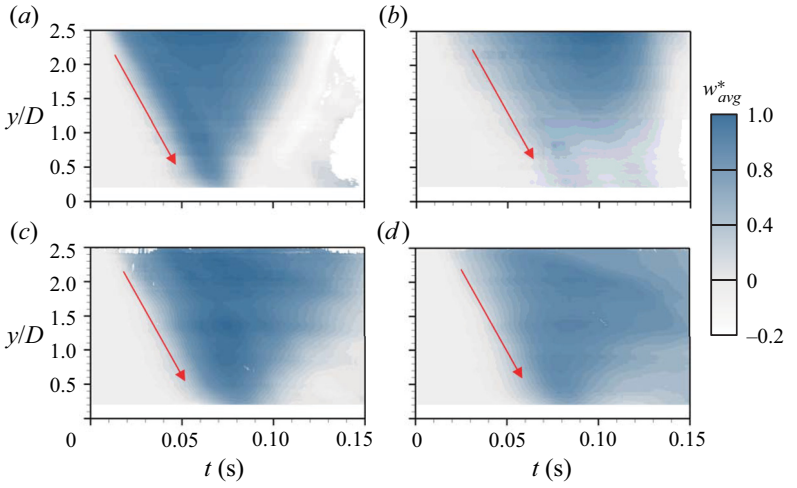

Figure 11. Spatio-temporal contour of the averaged nozzle displacement ($w^*_{avg} = (w^*_{left} + w^*_{right})/2$) with acceleration time (*a*,*b*) and jet Reynolds number: (*a*) $T_{acc} = 0.20$ s; (*b*) 0.22 s; (*c*) $Re_j = 6360$; (*d*) 12 555. For (*a*,*b*), $Re_j = 3286$ and $T_{acc} = 0.12$–0.13 s for (*c*,*d*). For all cases, the structural stiffness is fixed as $Eh = 7.0$ N m^{-1}. Here, the maximum displacement $w_{n,max}/D$ is given as (*a*) 0.036, (*b*) 0.031, (*c*) 0.081 and (*d*) 0.14.

nozzle is fully transferred to the kinetic energy of the ejecting jet when satisfying $t_{fc} = T_{acc}$, and this would incur the highest jet-exit velocity (figure 9*b*). Otherwise, for $t_{fc} < T_{acc}$ or $t_{fc} > T_{acc}$, the maximum jet-exit velocity decreases due to the early (figure 10*a*) or retarded (figure 10*c*) contraction of the nozzle, respectively.

As noted, the acceleration time (T_{acc}) is generally predetermined by the configuration of the motor–piston system; however, the instant of full contraction (t_{fc}) is determined by the jet–nozzle interaction. Because t_{cycle} can be understood as the time during which the travelling wave on the nozzle (which originally starts from the support of the nozzle at $y/D = 2.74$) comes back to its original position, it is expressed as $t_{cycle} = 2L/c$, where c and L denote the wave speed and the nozzle length, respectively. Thus, the above optimal condition can be written as $T_{acc}(= t_{fc}) = 3L/c$.

Before discussing theoretical aspects, notably, the measured data already indicate the strong dependency of the wave speed on the nozzle stiffness. Figure 11 shows the variation of w^*_{avg} depending on the acceleration time ($T_{acc} = 0.20$ and 0.22 s in figures 11*a* and 11*b*, respectively) and the terminal velocity of the jet (corresponding to $Re_j = 3286$ and 12 555 in figures 11*c* and 11*d*, respectively), while fixing the structural stiffness as $Eh = 7.0$ N m^{-1}. Note that the time in the figure is dimensional. During the expansion ($t < 0.05$ s) stage, the wave on the nozzle surface travels from the support to the tip (denoted as solid arrows in the figure), and, interestingly, its speed is almost independent of both T_{acc} and Re_j. This is contrary to the cases shown in figures 5 and 10, such that the wave speed significantly varies with nozzle stiffness; however, the only invariant parameter in figure 11 is the structural stiffness. Therefore, it can be speculated that the wave speed is determined by the material property rather than by the flow condition. To support this, quantitative measurements of the wave speed and its analytical analysis are provided in the following sections.

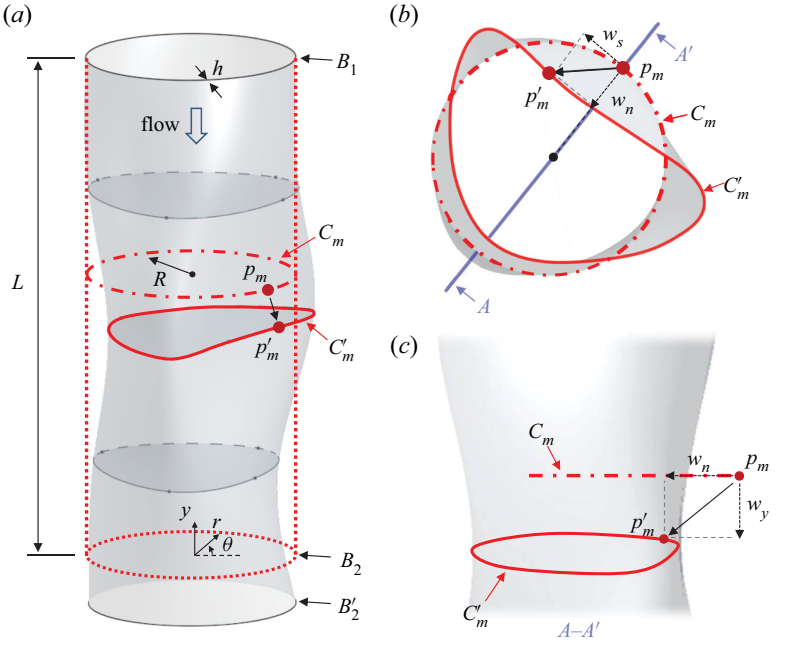

Figure 12. Schematic diagram of the deformed cylindrical shell: (*a*) isometric view; (*b*) top view; (*c*) view with respect to the plane (A–A') involving both the centre plane ($r = 0$) and the point p_m. The dashed lines denote the original circular cylinder before deformation. During deformation, the material curve C_m and the point p_m (on C_m) translate to the curve C'_m and point p'_m (on C'_m) with a displacement of $\boldsymbol{w} = (w_y, w_s, w_n)$. Note that the curve C'_m is not necessarily parallel to the r–θ plane.

4. Analytical formulation of the optimal flexibility condition

4.1. *Derivation of governing equations for nozzle deformation and jet velocity*

To construct equations for the fluid–structure interaction occurring in the present flexible circular nozzle, we defined the problem using the schematics of the deformed flexible nozzle in figure 12. Initially (without external forces), the nozzle has the shape of a circular cylinder (dashed line in figure 12*a*) with diameter D ($= 2R$), length L and thickness h. Here, the boundaries B_1 and B_2, respectively, correspond to the support and tip of the nozzle at the initial state. Global coordinates (r, θ, y) are defined with the origin at the centre of the nozzle tip. During deformation, the shape and location of support (B_1) remain fixed, but are not necessarily fixed for the tip (B_2) that is a free end. For the present set-up, the vertical location (y) of the nozzle tip changes slightly (maximum deviation of $0.2D$). Thus, we assume that the nozzle length is constant at L (the plane of B_2 and B'_2 is the same in figure 12*a*). As a result of deformation owing to the accelerated flow inside, we assume that the arbitrary material curve C_m on the nozzle is distorted to the curve C'_m; the point on curve C_m (denoted as point p_m) translates to point p'_m on C'_m (figure 12*a*). The displacement of p_m can be expressed as $\boldsymbol{w} = (w_y, w_s, w_n)$ (figure 12*b*,*c*). Here, the n and s axes are defined to be normal to the surface of the initial geometry and parallel to the θ axis, respectively (figure 12*b*). The radial direction outward from the nozzle is set to be positive, and the y axis is parallel to the direction of the nozzle length (figure 12*c*). To characterize the fluid flow inside the nozzle, the vector field of $\boldsymbol{v}(r, \theta) = (v_r, v_\theta, v_y)$ is considered on the arbitrary cross-sectional (normal to the y axis) planes of the deformed nozzle.

Because the material of the nozzle is impermeable, fluid flow inside the nozzle should satisfy mass conservation, and momentum conservation can also be formulated from the pressure distribution and surface force acting inside the nozzle. As we have shown, the nozzle deformation is assumed to be nominally axisymmetric ($w_s \simeq 0$) and both the radial and azimuthal velocity components are negligibly small, i.e. $\boldsymbol{v} \simeq (v_y, 0, 0)$. For the characteristic vertical velocity, on the other hand, the bulk velocity (u) is used, defined as $u = \int_S v_y \, \mathrm{d}A/S = Q/S$, where S and Q denote the arbitrary cross-sectional area normal to the y axis and the volume flux passing through S, respectively. Therefore, the conservation law for mass and momentum is expressed as follows (Shapiro 1977; Siviglia & Toffolon 2014):

$$\frac{\partial Q}{\partial y} + \frac{\partial S}{\partial t} = 0, \tag{4.1}$$

$$\frac{\partial Q}{\partial t} + \frac{\partial (uQ)}{\partial y} + \frac{S}{\rho_f}\frac{\partial p}{\partial y} = -Bu. \tag{4.2}$$

Here, t, ρ_f and p denote the time, fluid density and pressure difference between the outer and inner wall of the nozzle, respectively. The term on the right-hand side of (4.2) corresponds to the viscous friction on the inner wall of the nozzle, modelled as being linearly proportional to the bulk velocity with dimensional coefficient B. The cross-sectional area (S) and fluid flux (Q) can be calculated as $S = \pi(R + w_n)^2$ and $Q = uS = u\pi(R + w_n)^2$, respectively. Hence, (4.1) and (4.2) are written in terms of u and w_n ((4.3) and (4.4)):

$$\frac{\partial w_n}{\partial t} + \frac{R + w_n}{2}\frac{\partial u}{\partial y} + u\frac{\partial w_n}{\partial y} = 0, \tag{4.3}$$

$$\frac{\partial u}{\partial t} + u\frac{\partial u}{\partial y} + \frac{1}{\rho_f}\frac{\partial p}{\partial y} = -\frac{B}{\pi(R + w_n)^2}u. \tag{4.4}$$

The above equations can be solved if pressure p is determined based on the physical relation to the nozzle deformation and fluid flow, which is known as the 'tube law' (Siviglia & Toffolon 2014). Meanwhile, based on the assumption of axisymmetric deformation of the nozzle, the pressure can be analytically derived from the shell theory (detailed derivation is provided in Appendix B) as follows:

$$p = \frac{Eh}{R^2}w_n. \tag{4.5}$$

Equation (4.5) states that the pressure is linearly proportional to the radial displacement (w_n) with structural stiffness (Eh/R^2) as a proportional rate, resembling Hooke's law. When the jet accelerates, the pressure (p) at $y = y_p$ pushes the fluid volume at $0 < y < y_p$, which is accelerated with acceleration a towards the nozzle exit. Considering the control volume surrounded by the inner walls of the nozzle and the planes $y = y_p$ and $y = 0$, the change in the vertical momentum is determined by the difference in the pressure on the planes $y = 0$ and $y = y_p$, and the viscous friction (τ_w) on the inner wall, expressed as $\rho_f(\pi R^2 y_p)a = (\pi R^2)\Delta p - \tau_w(2\pi R y_p)$. For accelerating pipe flow, the unsteady wall-shear stress was obtained as $\tau_w = \rho_f a R(4\eta^{0.5} + 3\eta)/2$, where $\eta = t\nu_f/R^2$ (ν_f, kinematic viscosity of the fluid; t, time) (Annus *et al.* 2013). Thus, the ratio of inertia to pressure rise is expressed as

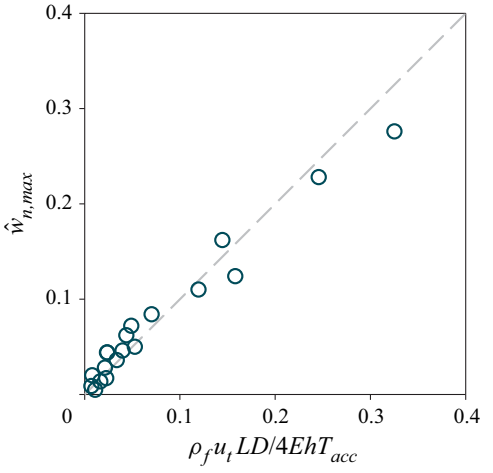

Figure 13. Comparison of the measured maximum radial displacement ($\hat{w}_{n,max} = w_{n,max}/D$) of the nozzle diameter with the prediction of (4.6).

$f_{in} = \rho_f(\pi R^2 y_p)a/(\pi R^2 \Delta p) = 1/(1 + 2\tau_w/(\rho_f aR)) = 1/(1 + 4\eta^{0.5} + 3\eta)$. This indicates that inertia solely determines the pressure rise initially, i.e. $f_{in} = 1.0$ at $t = 0$. As the jet accelerates, f_{in} slightly decreases to 0.85 in the middle of acceleration (at $t = 0.5T_{acc}$) when the frictional loss would be the largest. Thus, we may ignore the viscous stress for the whole process, and the expression for the pressure difference is reduced to $\Delta p = \rho_f y_p a$. Assuming that the reference pressure at the nozzle exit is zero, (4.5) is rewritten as $\rho_f a y_p = Ehw_n/R^2$. Here, the flow acceleration can be approximated as $a \simeq u_t/T_{acc}$. Because the maximum displacement ($w_{n,max}$) occurs near the support of the nozzle at $y_p \simeq L$ (see figure 5), $w_{n,max}/D$ can be obtained as follows:

$$\hat{w}_{n,max} = \frac{w_{n,max}}{D} = \frac{\rho_f u_j LD}{4EhT_{acc}}. \tag{4.6}$$

In figure 13, we compare the measured $w_{n,max}$ with that predicted by (4.6), which shows that the above analytical derivation is quite robust.

Confirming the reliability of (4.5), it is plugged into (4.3) and (4.4), and the resulting governing equations for mass and momentum conservation are derived as (4.7) and (4.8), respectively:

$$\frac{1}{\Pi_0}\frac{\partial \hat{w}_y}{\partial \hat{t}} + \hat{u}\frac{\partial \hat{w}_n}{\partial \hat{y}} = -\frac{1 + \hat{w}_n}{2}\frac{\partial \hat{u}}{\partial \hat{y}}, \tag{4.7}$$

$$\frac{1}{\Pi_0}\frac{\partial \hat{u}}{\partial \hat{t}} + \frac{\hat{u}}{(1 + \hat{w}_n)^2}\frac{\partial \hat{u}}{\partial \hat{y}} = -\Pi_1\frac{\partial \hat{w}_n}{\partial \hat{y}}. \tag{4.8}$$

Here, the variables were normalized as $\hat{y} = y/L$, $\hat{t} = t/T_{acc}$, $\hat{w}_n = w_n/R$ and $\hat{u} = u/u_t$, and the friction was neglected ($B = 0$). Equations (4.7) and (4.8) explain how nozzle displacement and bulk velocity of the fluid are correlated. Interestingly, two dimensionless parameters ($\Pi_0 = T_{acc}u_t/L$ and $\Pi_1 = Eh/(\rho_f u_j^2 R)$) appear, the physical meanings of which (the effective acceleration time and the effective nozzle stiffness, respectively) were discussed in § 2.4. This supports our understanding that Π_0 and Π_1 dictate the fluid–structure interaction between the starting jet and deformable nozzle. For both

equations, the two terms on the left-hand side are similar to the material derivative ($\mathcal{D} = (1/\Pi_0)\partial/\partial\hat{t} + \hat{u}\partial/\partial\hat{y}$) because $\hat{w}_n < 0.1$ and $(1 + \hat{w}_n)^2 \simeq 1.0$, as shown in figure 13. Here, the effective acceleration time (Π_0) determines the relative contribution of the local acceleration ($\partial/\partial\hat{t}$) to the convection acceleration ($\hat{u}\,\partial/\partial\hat{y}$). This understanding is extended such that Π_0 plays a similar role to the Strouhal number characterizing the unsteadiness of the flow structures. Equations (4.7) and (4.8) explain that the rate of change in $\hat{w}_y$ and $\hat{u}$ ($\mathcal{D}\hat{w}_y$ and $\mathcal{D}\hat{u}$, respectively) is determined by the spatial gradient of the counterpart variables, $\partial\hat{u}/\partial\hat{y}$ and $\partial\hat{w}_y/\partial\hat{y}$, respectively. For example, a positive $\partial\hat{u}/\partial\hat{y}$ indicates that the nozzle should contract in diameter, i.e. $\mathcal{D}\hat{w}_y < 0$, to satisfy the mass conservation, which is consistent with (4.7). In contrast, in (4.8), a positive $\partial\hat{w}_y/\partial\hat{y}$ corresponds to $\partial p/\partial y > 0$ following (4.5). The favourable pressure gradient will accelerate the bulk velocity, which agrees with the equation. Notably, the acceleration of the flow inside the nozzle ($\mathcal{D}\hat{u}$) is correlated with the nozzle deformation ($\partial\hat{w}_y/\partial\hat{y}$) with the proportional coefficient of Π_1, which originates from the relation between the displacement and pressure in the flow.

4.2. *Description of optimal flexibility for maximum thrust generation*

To determine the optimal condition ($T_{acc} \simeq 3L/c$) for maximizing thrust generation, it is necessary to find the speed (c) of the wave travelling on the nozzle surface. However, the governing equations (4.7) and (4.8) are nonlinear partial differential equations that can not be easily solved analytically. Rather than calculating the exact solution for the wave speed, we found that the asymptotic approach can successfully estimate the wave speed in a reasonable manner. At the early stage of jet acceleration ($t/T_{acc} \ll 1.0$), the bulk velocity is smaller than the terminal velocity ($\hat{u} = u/u_t \ll 1.0$), and the nozzle deformation is also negligible ($\hat{w}_n = w_n/R < 0.2$). Therefore, the second terms on the left-hand sides of (4.7) and (4.8) can be ignored, resulting in

$$\frac{1}{\Pi_0}\frac{\partial\hat{w}_y}{\partial\hat{t}} + \frac{1}{2}\frac{\partial\hat{u}}{\partial\hat{y}} = 0, \tag{4.9}$$

$$\frac{1}{\Pi_0}\frac{\partial\hat{u}}{\partial\hat{t}} + \Pi_1\frac{\partial\hat{w}_n}{\partial\hat{y}} = 0. \tag{4.10}$$

Subtraction between (4.9) and (4.10), after they are differentiated in terms of $\hat{t}$ and $\hat{y}$, respectively, provides the equation for $\hat{w}_n$ (equation (4.11)), and a similar procedure can be performed to obtain the equation for $\hat{u}$ (equation (4.12)):

$$\frac{\partial^2\hat{w}_n}{\partial\hat{t}^2} - \frac{\Pi_1\Pi_0^2}{2}\frac{\partial^2\hat{w}_n}{\partial\hat{y}^2} = 0, \tag{4.11}$$

$$\frac{\partial^2\hat{u}}{\partial\hat{t}^2} - \frac{\Pi_1\Pi_0^2}{2}\frac{\partial^2\hat{u}}{\partial\hat{y}^2} = 0. \tag{4.12}$$

The resulting equations have the form of a one-dimensional wave equation; both $\hat{w}_n$ and $\hat{u}$ have identical relations with the same coefficient of $\Pi_1\Pi_0^2/2$. To extract the wave speed from the equation, a normal mode of the perturbation of $\hat{w}_n$ and $\hat{u}$ (expressed as $\hat{u}, \hat{w}_n \sim \exp[i(\hat{k}\hat{y} - \hat{\omega}\hat{t})]$, where $\hat{k}$ and $\hat{\omega}$ correspond to the normalized frequency and the wavenumber of the perturbation, respectively) is replaced in (4.11) and (4.12), resulting in

$i^2\hat{\omega}^2 - (\Pi_1\Pi_0^2/2)i^2\hat{k}^2 = 0$. Therefore, the dimensionless wave speed is as follows:

$$\hat{c} = \frac{\hat{\omega}}{\hat{k}} = \pm\sqrt{\frac{\Pi_1\Pi_0^2}{2}} = \pm\sqrt{\frac{EhT_{acc}^2}{\rho_f DL^2}}. \tag{4.13}$$

The dimensionless wave speed is determined by two dimensionless parameters that we derived from the governing equations (4.7) and (4.8). The effective acceleration time ($\Pi_0 = u_t T_{acc}/L$) is the non-dimensional jet velocity (u_t) normalized by the characteristic velocity (L/T_{acc}). In the meantime, $\Pi_1^{0.5}$ can be understood as the dimensionless wave speed such that $\Pi_1^{0.5} = \sqrt{Eh/(\rho_f u_t^2 R)} = (c_s/u_t)\chi^{0.5}$, where c_s and χ denote the wave velocity of the elastic material (Païdoussis 1998; Paak *et al.* 2013) and the mass ratio between the nozzle wall and fluid ($\chi = \rho_s h/(\rho_f R)$). Therefore, $\Pi_0\Pi_1^{0.5}$ physically indicates the ratio of the surface wave speed to the characteristic flow velocity, as $\hat{c} = c/(LT_{acc}^{-1})$.

In dimensional form, the wave speed can be rewritten as follows:

$$c = \hat{c}\frac{L}{T_{acc}} = \pm\sqrt{\frac{Eh}{\rho_f D}}. \tag{4.14}$$

This implies that the wave speed is independent of the jet velocity and the acceleration time, which is consistent with the observation in figure 11. The positive and negative signs, respectively, denote that the surface wave may propagate either downward ($-y$) or upward ($+y$). As the nozzle stiffness (Eh) increases and the fluid inertia ($\rho_f D$) decreases, the wave speed increases. Equation (4.14) can also be deduced as one of the limiting cases from the acoustic interaction between an elastic cylinder and contained fluid (Lin & Morgan 1956). If the sound speed (c_f) and fluid inertia ($\rho_f R$) are much greater than the wave speed on the nozzle surface (c) and the nozzle inertia ($\rho_s h$), two solutions of the wave with mode $n = 0$ (axisymmetric) can be expressed as $c_1^2 = E(1 + \nu^2/(2\chi))/(\rho_s(1 - \nu^2))$ and $c_2^2 = Eh/(2\rho_f R(1 + \nu^2/(2\chi)))$, where ρ_s and ν correspond to the nozzle density and Poisson's ratio, respectively, obtained from the linearized equation of a thin circular cylindrical shell and two equations regarding the wave propagation (Laplace equation) and the momentum conservation. The former solution (c_1) denotes the axial vibration due to the negligible fluid viscosity and the latter (c_2) corresponds to the radial vibration that is related to the present point of interest. For all cases in the present study, we found that $\chi > 46.9$ and $\nu^2 = 0.16$, so the latter solution is directly simplified to (4.14) since $\nu^2/(2\chi) \ll 1.0$.

To further validate our analysis, we directly measured the wave speed from the result of nozzle deformation (figures 5, 10 and 11); the time delay (T_{wave}) between the instants when the enlarged diameter reaches 50 % of its maximum at two locations of $y_1/D = 2.5$ and $y_2/D = 1.5$ is measured, and the wave speed is calculated as $c = (y_1 - y_2)/T_{wave}$. Figure 14 compares the measured wave speed with the prediction (4.14), which shows remarkable agreement. This supports our analysis such that the surface wave speed solely depends on the material property of the nozzle rather than on the jet conditions. Additionally, we observed that the wave is faster than the terminal velocity of the jet ($u_t = 0.20$–0.84 m s^{-1}), implying that there exist two characteristic velocities for the starting jet issuing from a flexible nozzle.

Now, the optimal condition ($T_{acc} \simeq 3L/c$) for maximum thrust can be expressed with two non-dimensional parameters (Π_0 and Π_1) representing the flow and nozzle conditions, respectively, by substituting the relation for surface wave speed. The resulting relation is

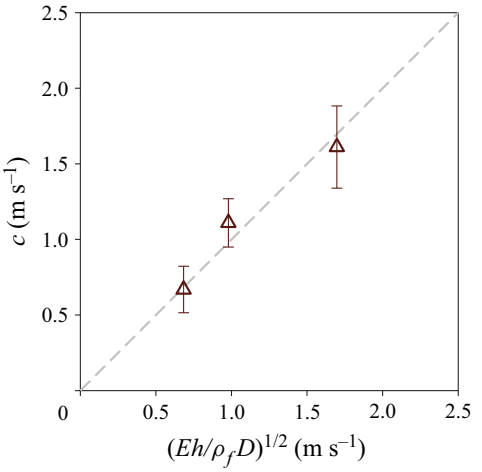

Figure 14. Validation of the wave speed (c) on the nozzle wall with the prediction of (4.14).

given as

$$\hat{c} = c\frac{T_{acc}}{L} = \sqrt{\frac{\Pi_1 \Pi_0^2}{2}} \simeq 3.0. \tag{4.15}$$

As noted, the optimized value of the dimensionless wave speed is given together, which is ∼3.0 for the present configuration. To confirm the validity of condition (4.15), we have plotted all the considered cases in the parameter space of Π_0 and Π_1 in figure 15(a) (optimal condition (4.15) is shown as a dashed line in the figure). Clearly, the cases with a larger thrust lie on the line $\hat{c} = 3.0$. As we analysed above, for $\hat{c} > 3.0$ (above the dashed line in figure 15a), the wave speed is relatively fast so that the full contraction is completed before jet acceleration ends (see figure 10). Because the nozzle releases its elastic energy before the jet reaches the maximum velocity, the timing mismatch weakens thrust generation (figure 9c). On the other hand, for $\hat{c} < 3.0$, the response of the nozzle to the acceleration is too slow, forcing the nozzle to contract after the acceleration finishes, which also produces weaker thrust.

Figure 15(b) shows the relative impulse ($\hat{I}_h$) depending on the dimensionless wave speed ($\hat{c}$) for the same dataset shown in figure 15(a). The impulse is measured at $t/T_{acc} = 1.0$ and normalized with the value from the rigid nozzle, expressed as $\hat{I}_h|_{t=T_{acc}} = I_h/I_{h,rigid}|_{t=T_{acc}}$. Clearly, the impulse increases as $\hat{c}$ approaches 3.0 from both regimes of $\hat{c} > 3.0$ and $\hat{c} < 3.0$. Interestingly, for the cases of $\hat{c} \simeq 3.0$ (denoted with symbols with cross marks), the amplification of the relative impulse is not identical but tends to increase with increasing effective stiffness, Π_1 (or tends to decrease with increasing effective acceleration time, Π_0): e.g. $\hat{I}_h|_{t=T_{acc}} = 1.35$ (for $\Pi_1 = 2.74$), 1.47 (4.72), 1.77 (10.68) and 2.07 (19.45).

4.3. *Scaling law for optimal flexibility*

The enhancement in thrust (figure 15b) comes from the elastic potential energy (P) transferred to the kinetic energy of the fluid flow inside the nozzle during contraction. The elastic potential energy is expressed in terms of the deformation amplitude (w_n) as

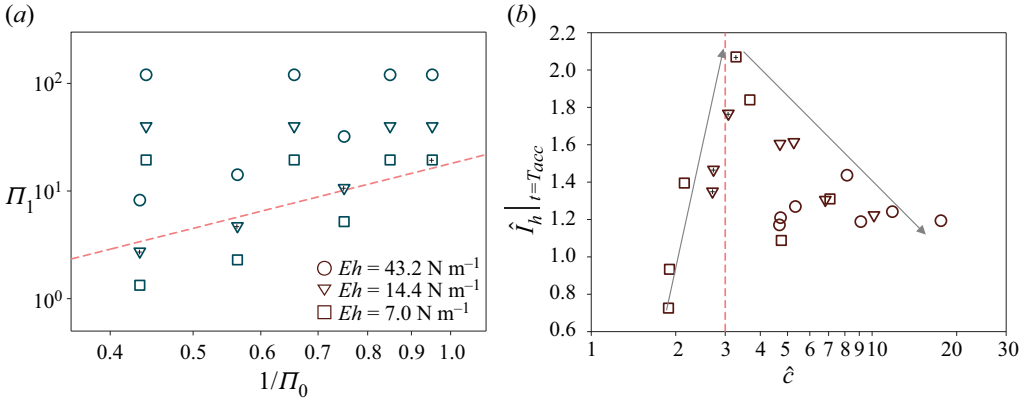

Figure 15. (*a*) Regime map (Π_0–Π_1) and (*b*) impulse generation depending on the dimensionless wave speed ($\hat{c}$) for all cases tested in the present study. The dashed lines correspond to $\hat{c} = 3.0$, and the symbols with cross marks denote the cases near the optimal condition.

(Kraus 1967)

$$P = \int_0^L \int_0^{2\pi} \frac{1}{2} N_{ss} w_n \, \mathrm{d}\theta \, \mathrm{d}y. \tag{4.16}$$

Here, N_{ss} corresponds to the tensile stress in the azimuthal direction (see the detailed definition and its derivation in Appendix C). Considering that (i) the nozzle expands predominantly in the radial direction ($\hat{w}_n \gg \hat{w}_y$), (ii) the deformation is axisymmetric and (iii) the relation between pressure and radial displacement (4.6) holds, the elastic energy can be rewritten as (the detailed procedure of derivation is given in Appendix C)

$$P \simeq \frac{\pi R^3 a^2 \rho_f^2 L^3}{3(1-\nu^2)Eh}. \tag{4.17}$$

The acceleration is approximated as $a \simeq u/T_{acc}$, and ν denotes Poisson's ratio of the nozzle material. Meanwhile, the kinetic energy (M) of the jet is calculated as $M = \rho_f(\pi R^2 L)u^2/2$, and its increment ($\Delta M$) corresponding to the change in jet velocity (Δu) is obtained as $\Delta M = \Delta(\rho_f \pi R^2 L u^2/2) = \rho_f \pi R^2 L(u\Delta u)$.

Using the experimental data, it is possible to examine the transfer of elastic potential energy of the nozzle to jet kinetic energy. The elastic potential energy (P) of the nozzle deforming axisymmetrically with a normal displacement (w_n) is calculated as $P = \pi EhR/(1-\nu^2)\int_0^L (w_n/R)^2 \mathrm{d}y$ ((C4) in Appendix C), which is further non-dimensionalized as $\hat{P} = P/(\pi EhRL)$. Meanwhile, the kinetic energy (E_k) of the axisymmetric and non-swirling flow can be calculated as $E_k = 0.5\pi\rho_f \int_C r(u^2+v^2)\,\mathrm{d}A$ (Saffman 1995; Limbourg & Nedić 2021*a*), where the control surface (C) is the same as that used for calculating Γ (figure 7*a*), which corresponds to the flow domain below the nozzle exit ($y < 0$). Here, u and v denote the horizontal and vertical velocity, respectively. The normalized kinetic energy is defined as $\hat{E}_k = E_k/(\rho_f u_t^2 D^3)$. Figure 16 shows the time history of $\hat{E}_k$ and $\hat{P}$ depending on the structural stiffness (Eh). For the rigid nozzle ($Eh = \infty$), the kinetic energy starts to increase gradually from $t = 0$; however, for the flexible nozzles, it starts to increase at delayed instants of $t/T_{acc} = 0.16$ (for $Eh = 43.2$ N m^{-1}), 0.21 (14.4 N m^{-1}) and 0.31 (7.0 N m^{-1}), agreeing with the instants

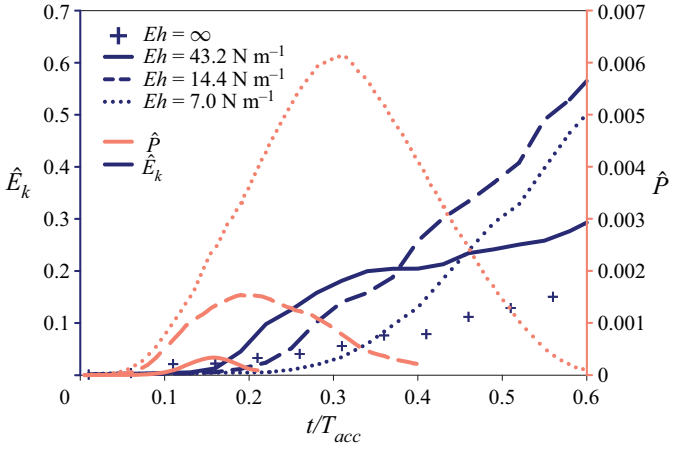

Figure 16. Time history of jet kinetic energy ($\hat{E}_k = E_k/(0.5\rho_f u_t^2 D^3)$) and elastic potential energy ($\hat{P} = P/(\pi EhLR)$) of the flexible nozzle depending on Eh.

when the corresponding potential energy reaches its maximum value and decreases. This clearly indicates that the elastic potential energy is transferred to the jet kinetic energy during nozzle deformation. The stored elastic potential energy increases with decreasing Eh, implying that the optimally flexible nozzle can attain the largest amount of elastic energy from the accelerating jet. For the same reason, the growth rate of jet kinetic energy becomes steeper as Eh decreases. If the stored potential (elastic) energy is fully converted to kinetic energy of the jet (i.e. $\Delta M \sim P$) during the contraction of the nozzle, the increase in the jet velocity can be obtained by combining (4.17) and the relation for ΔM (see the detailed derivation in Appendix D):

$$\frac{\Delta u}{u} \sim \frac{\Pi_0^2}{\Pi_1} \sim \frac{1}{\hat{c}^2}. \tag{4.18}$$

Equation (4.18) implies that the change in the jet velocity is also related to the effective acceleration time ($\Pi_0 = T_{acc} u_t/L$) and effective stiffness ($\Pi_1 = Eh/\rho_f u_j^2 R$). The increase in the jet velocity is further scaled as $\Delta u/u \sim 1/\hat{c}^2$, indicating that the maximum velocity would remain unchanged if two dimensionless parameters satisfy the optimal condition ($\hat{c} = 3.0$). This is different from the result shown in figure 15(b), where the jet impulse varies although the dimensionless wave speed converges to a value of 3.0.

We believe that this discrepancy originates from the assumption that the entire elastic energy is transferred to the kinetic energy of the jet ($\Delta M \sim P$) during acceleration of the jet. In figures 10(b) and 10(c), we can see that the duration of nozzle contraction is longer than that of nozzle expansion. Other evidence is that the temporal variation of the averaged nozzle diameter for the three cases satisfying $\hat{c} \simeq 3.0$ (denoted as symbols with cross marks in figure 15) is shown in figure 17. The wave speeds along the expansion stage (denoted as dotted arrows in the figure) seem to be identical to each other because the dimensionless wave speed is very similar to that of the optimal value. In the contraction stage (denoted as solid arrows in the figure), however, the nozzle contracts more slowly as Π_0 increases (or Π_1 decreases). This is because the accelerated flow inside the nozzle involves the process of wave propagation (i.e. fluid–structure interaction). This does not occur when contraction ends far before acceleration ends

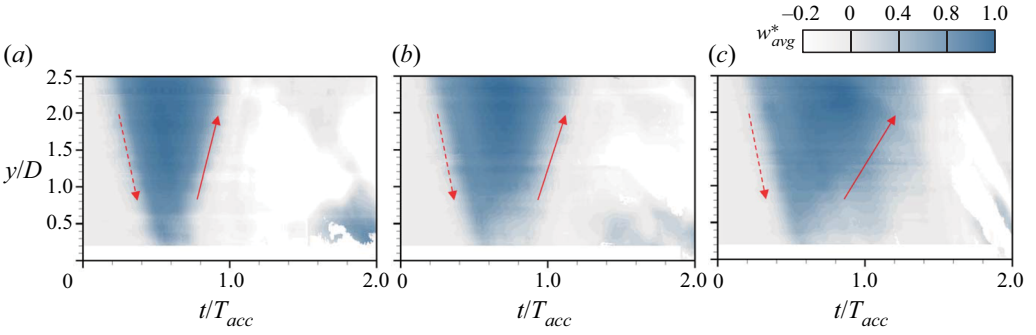

Figure 17. Spatio-temporal contour of the averaged nozzle displacement ($w^*_{avg} = (w^*_{left} + w^*_{right})/2$) for cases satisfying the optimal condition: (*a*) $\hat{c} = 3.08$ ($\Pi_0 = 1.33$, $\Pi_1 = 10.7$); (*b*) 2.73 ($\Pi_0 = 1.79$, $\Pi_1 = 4.72$); (*c*) 2.70 ($\Pi_0 = 2.33$, $\Pi_1 = 2.74$). Here, $Eh = 14.4$ N m^{-1} and $T_{acc} = 0.12$–0.13 s for all cases. Here, the maximum displacement $w_{n,max}/D$ is given as (*a*) 0.042, (*b*) 0.055 and (*c*) 0.062.

($t/T_{acc} \ll 1.0$). For this condition, the durations of both expansion and contraction are identical because the assumption for jet velocity ($u \simeq 0$) in (4.9) and (4.10) is valid, as shown
in figure 5.

To model this decelerated wave speed, we revisit the governing equations that we derived for the nozzle deformation and jet speed. Let us consider the surface wave moving downward ($-y$) while the jet velocity saturates to $u = u_t$. A small perturbation on the jet velocity (u_p) is introduced as $\hat{u} = 1 + \hat{u}_p$ (note that a hat denotes normalization with u_t). Based on the observation that the radial displacement is small compared with the nozzle radius ($\hat{w}_n = w_n/R \ll 1$), (4.7) and (4.8) are reduced to

$$\mathcal{D}\hat{w}_n + \frac{1}{2}\frac{\partial \hat{u}_p}{\partial \hat{y}} = 0, \tag{4.19}$$

$$\mathcal{D}\hat{u}_p + \Pi_1 \frac{\partial \hat{w}_n}{\partial \hat{y}} = 0. \tag{4.20}$$

Here, the differential operator $\mathcal{D}$ is defined as $\mathcal{D} = (1/\Pi_0)\partial/\partial\hat{t} + \partial/\partial\hat{y}$, and the higher-order terms are ignored. Then, through similar procedures to construct single-variable equations, the above equations can be rearranged as follows:

$$\mathcal{D}^2\hat{w}_n - \frac{\Pi_1}{2}\frac{\partial^2 \hat{w}_n}{\partial \hat{y}^2} = 0, \tag{4.21}$$

$$\mathcal{D}^2\hat{u}_p - \frac{\Pi_1}{2}\frac{\partial^2 \hat{u}_p}{\partial \hat{y}^2} = 0. \tag{4.22}$$

As expected, $\hat{w}_n$ and $\hat{u}_p$ are the solutions of the same wave equation. By substituting the normal mode of perturbation defined as $\hat{u}_p, \hat{w}_n \sim \exp[i(\hat{k}\hat{y} - \hat{\omega}\hat{t})]$, the dispersion relation appears as $(1/\Pi_0^2)\hat{\omega}^2 - (2/\Pi_0)\hat{k}\hat{\omega} + (1 - \Pi_1/2)\hat{k}^2 = 0$. Using the quadratic formula for frequency ($\hat{\omega}$), the reduced wave speed ($\hat{c}_r$) is obtained in both dimensionless (4.23) and

dimensional (4.24) forms, respectively,

$$\hat{c}_r = \frac{\hat{\omega}}{\hat{k}} = \Pi_0(1 \pm \sqrt{\Pi_1/2}), \tag{4.23}$$

$$c_r = \frac{\hat{c}_r L}{T_{acc}} = u_t(1 \pm \sqrt{\Pi_1/2}) = u_t \pm \sqrt{\frac{Eh}{\rho_f D}} = u_t \pm |c|. \tag{4.24}$$

The negative sign corresponds to the jet direction. According to (4.24), the wave speed is not only affected by the effective nozzle stiffness but is also augmented by the jet terminal velocity (u_t), unlike (4.13) and (4.14). A similar formulation was reported for the free vibrations of a fluid-conveying shell (Chen & Rosenberg 1974). From the shell equation without assuming a thin shell, i.e. Flügge equation, and the fluid momentum conservation equation, the water-hammer wave speed with vibration of $n = 0$ (axisymmetric mode) can be calculated as $u_t \pm c_f/\sqrt{1 + 2KR/(Eh)}$, where K and c_f denote the fluid's bulk modulus and wave speed, respectively. Because $K = \rho_f c_f^2$, this relation can be rewritten as $u_t \pm 1/\sqrt{(1/c_f^2 + 2\rho_f R/(Eh)} = u_t \pm 1/\sqrt{1/c_f^2 + 1/c^2}$, which is directly reduced to (4.24) under the condition of $c^2/c_f^2 \ll 1$. Thus, relation (4.24) corresponds to the case in which acoustic waves decouple. Next, the wave speed in the upward direction is $c_{r,u} = u_t + |c|$ (note that u_t has a negative sign). Therefore, the effective time duration corresponding to the release of the elastic energy stored in the expanded nozzle (T_{eff}) is calculated with the reduced wave speed as $T_{eff} = L/c_{r,u}$. Accordingly, the energy balance used to derive (4.18) can be modified such that the emitted potential (elastic) energy of the nozzle contributes to the generation of maximum thrust during the acceleration time (T_{acc}) only. This can be considered as follows:

$$\Delta M \sim P\frac{T_{acc}}{T_{eff}}. \tag{4.25}$$

Substituting the relation for ΔM, P and T_{eff}, the equation for the change in the jet velocity is rewritten as follows (the detailed derivation can be found in Appendix D):

$$\frac{\Delta u}{u} \sim 1 - \sqrt{\frac{2}{\Pi_1}} = J^*. \tag{4.26}$$

The scaling relation (4.26) indicates that if the nozzle material and the jet characteristics satisfy the optimal condition (i.e. $\hat{c} = 3.0$), the maximum jet velocity increases with increasing effective stiffness (Π_1). While validating the modified argument on the transfer of elastic energy to the jet kinetic energy, figure 18 clearly shows that both the augmentation in jet velocity and the impulse for the cases around the optimal condition ($1.5 < \hat{c} < 4.5$) are well correlated with J^*. For the off-optimal condition ($\hat{c} > 4.5$), flow variables related to thrust show poor correlation with J^*. Another implication that we can learn from J^* is that there is an upper limit of $J^* \to 1.0$ as $\Pi_1 \to \infty$. That is, increasing the nozzle stiffness will saturate the thrust to a certain value (under the condition that the jet and the nozzle satisfy the optimal condition). In figure 18(a), extrapolation of the optimal condition (denoted as dashed arrows) predicts that the augmented velocity will be approximately 131 % (236 % for the hydrodynamic impulse) larger than that of the rigid nozzle. Unfortunately, the limitation in manufacturing thinner nozzles than those tested and the faster response time of the motor specification did not allow us to explore the corresponding regime of $J^* \simeq 1.0$. Together with (4.15), (4.26) raises the

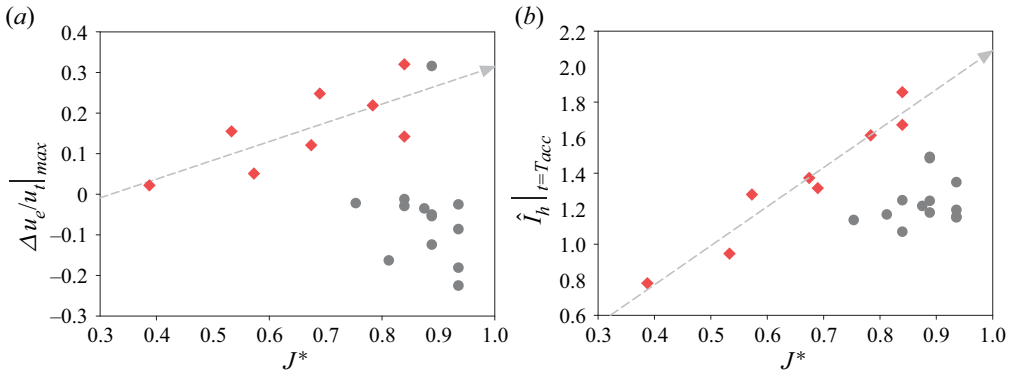

Figure 18. (*a*) The maximum increase of jet-exit velocity ($\Delta u_e/u_t|_{max}$) and (*b*) the relative hydrodynamic impulse at $t = T_{acc}$ depending on J^*: ♦, $1.5 < \hat{c} < 4.5$; •, $\hat{c} > 4.5$. The dashed lines are the extrapolation curves of $a_1 J^* + a_2$, where $(a_1, a_2) = (0.46, 0.15)$ (*a*) and $(2.75, 0.38)$ (*b*).

important implication that thrust generation must be treated for understanding the optimal condition (which considers the ratio between the structural response time and flow time scale) and the mechanism of the delayed release of the flexible nozzle (which stems from the slower surface wave speed with decreasing effective stiffness). Without this consideration, misinterpretations can occur; for example, reduced stiffness either enhances the impulse generation (as observed in figure 7) or, totally conversely, reduces it (as shown in figure 18*b*). This will be useful for understanding and predicting thrust generation from a flexible nozzle, which is prevalent in nature and industrial applications.

5. Concluding remarks

We conducted an experimental and analytical investigation of the evolution of a starting jet through a flexible circular nozzle. The flexible nozzles are manufactured with three different structural stiffnesses, and the terminal velocity of the jet and acceleration time are systematically adjusted using an in-house piston–motor system. To understand the dynamics of the jet structure in time and space, we performed two-dimensional PIV measurements, and measured the deformation of the nozzle surface together with subpixel image processing. The evolution of the flow field shows that the primary vortex shed from the nozzle exit convects faster as the nozzle is more flexible; consequently, the hydrodynamic thrust increases approximately 90 % greater than that of the rigid nozzle. Based on the quantification of nozzle deformation, we found that the expansion and contraction of the nozzle, respectively, accumulates the elastic potential energy and transfers it to the flow inside the jet, thereby increasing the jet velocity inside the nozzle. This is the key fluid–structure interaction mechanism responsible for maximizing thrust generation. To characterize the interaction between the flexible nozzle and the accelerating flow in it, the governing equations for the nozzle deformation and flow velocity are derived from the shell theory and conservation laws for mass and momentum, in which two dimensionless parameters, i.e. effective acceleration time (Π_0) and effective nozzle stiffness (Π_1), are used. The subsequent analytical investigation, supported by the measured flow field and nozzle deformation, indicates that the time when the contraction completely ends has to be comparable to the instance when the jet reaches maximum velocity, to produce maximum thrust. This optimal condition is expressed as

$\hat{c} = \sqrt{\Pi_0^2 \Pi_1/2} \simeq 3.0$, where $\hat{c}$ is the dimensionless surface wave speed. While satisfying this condition, furthermore, the maximum jet velocity of the flexible nozzle depends on the effective nozzle stiffness (Π_1), which is attributed to the reduced wave speed drawn by asymptotic analysis. The augmentation in the jet-exit velocity is found to increase with effective stiffness, which is scaled as $\Delta u/u \sim 1 - \sqrt{2/\Pi_1}$.

Therefore, we understand that the flexibility of the nozzle has the potential not only for thrust improvement in jet flow but also for the agility of the system. Numerous organisms and industrial applications make use of a flexible nozzle, which ejects an impulsively starting jet. Thus, it will be fascinating to examine if jet conditions (i.e. the terminal velocity and the acceleration time) and the material property of the nozzle (i.e. Young's modulus and thickness) follow the optimal condition derived in the present study. In addition, the dimensionless surface wave speed (it was approximately 3.0 for the circular nozzle) must be quantified, depending on the nozzle geometry such as a cone-shaped nozzle.

Supplementary material. Supplementary material is available at https://doi.org/10.1017/jfm.2022.781.

Funding. This work was supported by a research grant (20210584) through the Korea Institute of Marine Science & Technology Promotion funded by Korea Coast Guard, research grants (2020R1A2C2014510, 2021R1A4A1032023) through the National Research Foundation of Korea funded by the Korean government (MSIT), a Korea Medical Device Development Fund grant (no. HW20C2103) and Institute of Engineering Research at Seoul National University.

Declaration of interests. The authors report no conflict of interest.

Author ORCIDs.
Hyungmin Park https://orcid.org/0000-0003-3525-8573.

Appendix A. Nozzle exit deformation after acceleration ($t/T_{acc} > 1$)

The nozzle exit deformation after T_{acc} is briefly outlined here. In § 3.1, we showed that two-dimensional edge detection has its limitation after expansion–contraction stage (figure 5) because the deformation is three-dimensional (figure 6*g*,*h*). To investigate the dynamics of the nozzle tip for various conditions, the tip deformation was measured for three jet conditions ($Re_j = 3600$, 7200 and 9300) and three nozzle flexibilities ($Eh = 7.0$, 14.4 and 43.2 N m^{-1}), using a high-speed camera with a resolution of 720 × 712 pixels and an acquisition rate of 1000 Hz. Illuminated by the horizontal laser sheet, the nozzle tip could be identified as a bright closed curve (figure 19*a*), which is binarized using an in-house image-processing technique (figure 19*b*) to quantify the morphology. Figure 19 shows the time-varying deformation of the nozzle tip for $Eh = 43.2$ N m^{-1} and $Re_j = 9300$ at $t/T_{acc} = 3.2$–3.5. We observe that the triangular shape, i.e. the wavenumber (n) of 3, is salient at $t/T_{acc} = 3.2$ and evolves into a reversed triangle at $t/T_{acc} = 3.48$.

For quantitative analysis, the measured radial deformation in the azimuthal direction at each time (see the polar coordinate in figure 19*b*) can be expressed as the sum of waves with modes $n > 0$, using the Fourier transform. Figure 20 shows the temporal variation of amplitude of each wave for $Re_j = 3600$–9300 and $Eh = 7.0$–43.2 N m^{-1}. When the jet velocity is low ($Re_j = 3600$) and the nozzle is stiffer ($Eh = 43.2$ N m^{-1}), the nozzle shape is static (figure 20*a*) and the amplitudes are negligible. Thus, the nozzle tip remains in its original shape as a circle at all times. However, increasing the jet velocity ($Re_j = 7200$–9300 and $Eh = 43.2$ N m^{-1}; figure 20*b*,*c*), the periodic

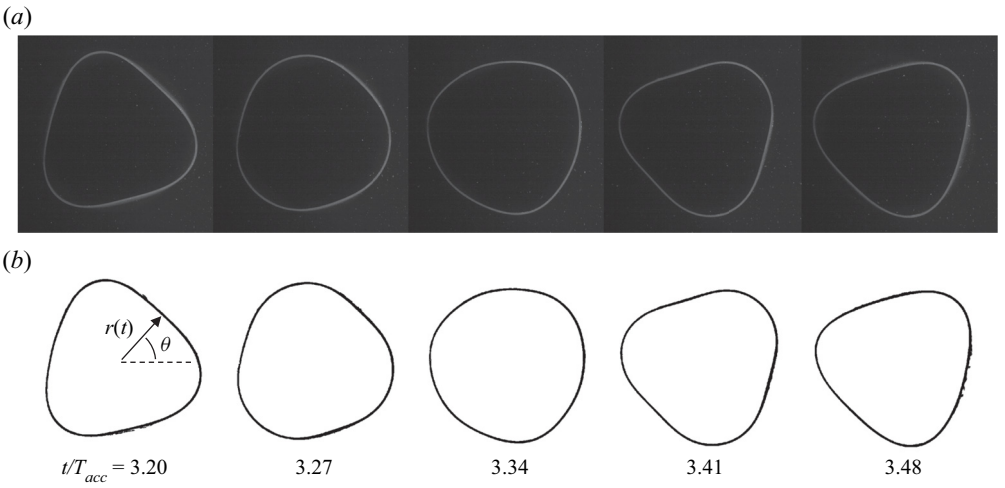

Figure 19. (*a*) The time-varying tip deformation of the flexible nozzle for $Eh = 43.2$ N m^{-1} and $Re_j = 9300$ at $t/T_{acc} = 3.2$–3.5 with (*b*) the binarized images.

oscillation with mode $n = 3$ is manifested after the acceleration ($t/T_{acc} > 1$), while interestingly, a rectangular oscillation appears for the stiffer nozzle when $Re_j = 7200$ and $Eh = 14.4$ N m^{-1} (figure 20*e*). On the other hand, the mixed modes $n = 3$ and 4 occur at the lowest velocity ($Re_j = 3600$) and softer nozzles ($Eh = 7.0$–14.4 N m^{-1}) in figures 20(*d*) and 20(*g*) at $t/T_{acc} > 1$. Finally, for the highest Reynolds numbers and softer nozzles (figure 20*f*,*h*,*i*), the wave amplitudes become weaker, possibly owing to (i) the irregular deformation resulting from the interaction between multiple modes and (ii) the development of the wave in the longitudinal direction which disrupts the formation of an organized deformation pattern. Note that there is a difficulty in evaluating the higher modes ($n > 4$) owing to their smaller amplitude compared with the lower modes ($n < 4$). For example, at $t = T_{acc}$, the nozzle generally experiences buckling, characterized by wrinkles of the tip ($n \simeq 7$ in figure 6*f*), which cannot be extracted clearly from the present resolution.

The modal deformation of a thin nozzle with internal flow can be predicted using the nonlinear shell theory that accounts for the large nozzle deformation and viscous structural damping (Païdoussis & Denise 1972; Païdoussis 1998; Paak *et al.* 2013). It was reported that the periodic deformation of the azimuthal mode ($n = 3$) occurs for similar geometric conditions of $L/D = 3$, $h/R = 0.02$ (Paak *et al.* 2013), while our cases correspond to $L/D = 2.74$ and $h/R = 0.021$ for figures 20(*b*) and 20(*c*). However, there is a discrepancy in the bulk velocity inside the shell ($u_r = u_b/c_s$, where u_b and c_s denote the fluid bulk velocity and the material velocity, $c_s = E/(\rho_s(1 - \nu^2))$, respectively): $u_r = 0.5$ for Paak *et al.* (2013) and 0.028–0.036 for the present work. In that previous work, the shell became unstable at $u_r > 0.42$, while $u_r = 0.013$ was sufficient to excite the self-oscillation of the flexible nozzle in the present study. The early onset of vibration may originate from the initial non-ideal conditions of the nozzle and inflow. The deformation of the nozzle at $t/T_{acc} = 2$–4 begins with energetic contraction motion at $t/T_{acc} \simeq 1$, which is large enough to cause the dynamic system to reach another equilibrium state. For the present starting jet condition, it did not allow observation of the oscillation for a long period ($t/T_{acc} > 10$) due to the finite length of the ejected fluid slug. On the other hand, it

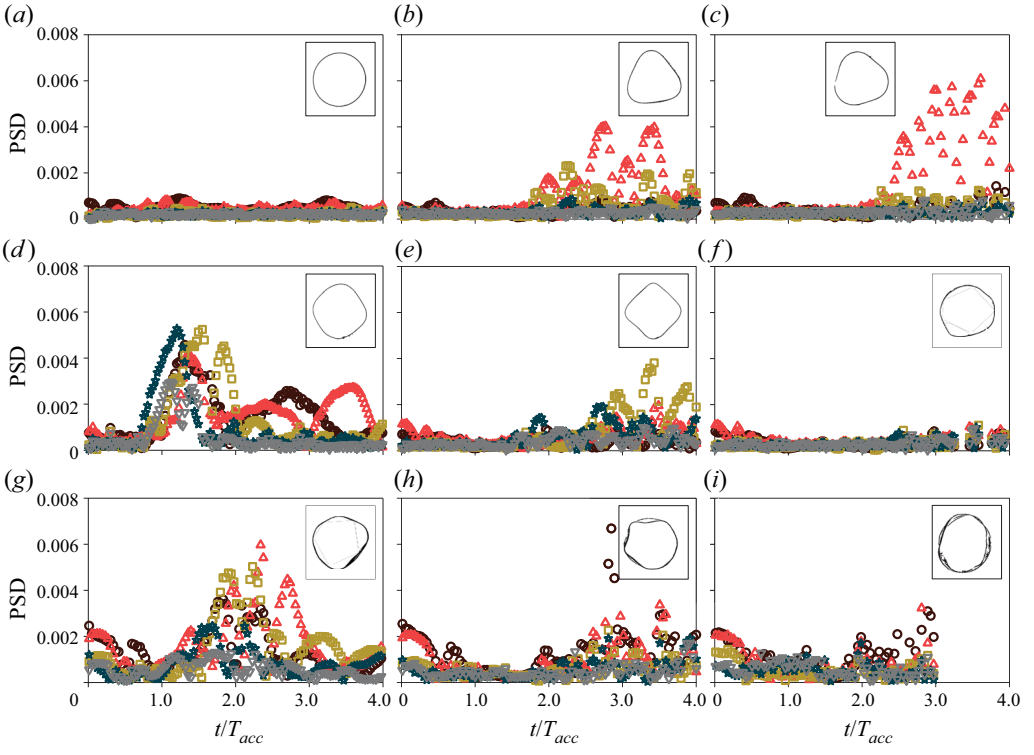

Figure 20. Temporal variation of the wave amplitude with mode $n = 2$ (○); 3 (△); 4 (□); 5 (⋆); 6 (▽). For the operating conditions, the jet Reynolds number (Re_j) is 3600 (*a–c*), 7200 (*d–f*) and 9300 (*g–i*), and the structural stiffness (Eh) is 43.2 N m^{-1} (*a*,*d*,*g*), 14.4 N m^{-1} (*b*,*e*,*h*) and 7.0 N m^{-1} (*c*,*f*,*i*). The insets show representative images of tip deformation.

was found that the fluid velocity at $t/T_{acc} > 1$ slightly oscillates (oscillation amplitude is approximately 6.8 % of u_t), thus indicating that inherent perturbation exists in the inlet condition.

Appendix B. Derivation of pressure distribution using the shell theory

To determine the flow bulk velocity (u) and nozzle deformation (w_n) from (4.7) and (4.8), it is necessary to elucidate the relation between the pressure and the displacement, i.e. the tube law. The deformation of the thin flexible nozzle can be assumed as the motion of a cylindrical shell with a uniform thickness (Kraus 1967). Assuming that the nozzle is thin enough (less than approximately 10 % of the nozzle diameter) and the deformation is small enough for the material to follow Hooke's law (Love 1888), the infinitesimal element of the elastic material is governed by the theory of thin elastic shell (the orientation of each force and moment is given in figure 21):

$$\frac{\partial N_{yy}}{\partial y} + \frac{\partial N_{ys}}{\partial s} + q_y = \rho_n h \frac{\partial^2 w_y}{\partial t^2}, \tag{B1}$$

$$\frac{\partial N_{ys}}{\partial y} + \frac{\partial N_{ss}}{\partial s} + \frac{N_{sn}}{R} + q_s = \rho_n h \frac{\partial^2 w_s}{\partial t^2}, \tag{B2}$$

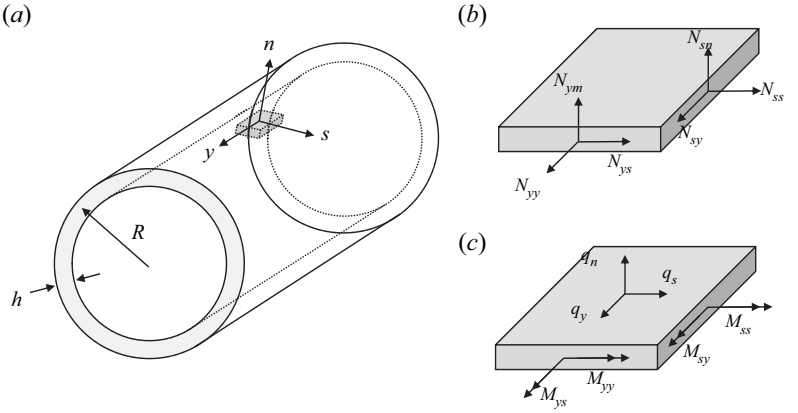

Figure 21. Schematic diagrams showing (*a*) the infinitesimal element in the thin flexible nozzle on which the reference coordinates (y, n, s) are defined, (*b*) the edge forces and (*c*) the edge moments and external surface forces on the element in (*a*).

$$\frac{\partial N_{yn}}{\partial y} + \frac{\partial N_{sn}}{\partial s} - \frac{N_{ss}}{R} - q_n = \rho_n h \frac{\partial^2 w_n}{\partial t^2}, \tag{B3}$$

$$\frac{\partial M_{ys}}{\partial y} + \frac{\partial M_{yy}}{\partial s} - N_{yn} = 0, \tag{B4}$$

$$\frac{\partial M_{yy}}{\partial y} + \frac{\partial M_{sy}}{\partial s} - N_{sn} = 0. \tag{B5}$$

Here, N_{ij} and M_{ij} denote the resultant stress and the stress couple (i.e. moment), respectively, in the direction of the j axis acting on the surface normal to the i axis $(i, j = y, s, n)$. Here, y, s and n represent the components parallel to the nozzle length, circumference and normal to the nozzle wall, respectively (figure 21), and t is time. Parameters q_i and w_i denote the external force acting on the nozzle surfaces and the displacement in the i direction, respectively, and ρ_n, R and h are the density, radius and thickness of the nozzle, respectively. Equations (B1)–(B3) correspond to Newton's second law along each axis and (B4) and (B5) state the balance of the moment in the y and s directions (here, the equation in the n direction is omitted since it is automatically satisfied by the symmetry of the stress tensors).

If the nozzle is thin enough (membrane state), the moment on the nozzle wall can be ignored, resulting in $N_{yn} = N_{sn} = 0$ according to (B4) and (B5). Since the deformation of the nozzle is axisymmetric during the acceleration time ($\partial/\partial s = 0$ and $w_s = q_s = 0$), (B1)–(B3) are reduced to (B6)–(B8):

$$\frac{\partial N_{yy}}{\partial y} + q_y = \rho_n h \frac{\partial^2 w_y}{\partial t^2}, \tag{B6}$$

$$\frac{\partial N_{ys}}{\partial y} = 0, \tag{B7}$$

$$-\frac{N_{ss}}{R} - q_n = \rho_n h \frac{\partial^2 w_n}{\partial t^2}. \tag{B8}$$

Equation (B7) can be integrated to have $N_{ys} = 0$ since the stress vanishes at the nozzle tip ($y = 0$). Therefore, the nozzle deformation is governed by (B6) and (B8). Following Love's postulates that state that the normal stress is negligible and the normal vector to the nozzle surface remains unchanged (i.e. $\epsilon_n = \gamma_{yn} = \gamma_{sn} = 0$, where ϵ and γ denote the normal and shearing strain), the following relations are obtained:

$$N_{yy} = \frac{Eh}{1-\nu^2}(\epsilon_y + \nu\epsilon_s), \tag{B9}$$

$$N_{ss} = \frac{Eh}{1-\nu^2}(\epsilon_s + \nu\epsilon_y), \tag{B10}$$

$$N_{sy} = N_{ys} = Gh\gamma_{ys}, \tag{B11}$$

$$\epsilon_y = \frac{\partial w_y}{\partial y}, \tag{B12}$$

$$\epsilon_s = \frac{\partial w_s}{\partial s} + \frac{w_n}{R}, \tag{B13}$$

$$\gamma_{xs} = \frac{\partial w_s}{\partial y} + \frac{\partial w_y}{\partial s}. \tag{B14}$$

Here, (B9)–(B11) and (B12)–(B14) denote the stress–strain and the strain–displacement relations, respectively. The elastic properties E, G and ν are the Young's modulus, shear modulus and Poisson's ratio, respectively. Equation (B11) vanishes since $N_{ys} = 0$ from (B7). Applying the assumption of axisymmetry immediately eliminates (B14) (since $w_s = 0$ and $\partial/\partial s = 0$) and reduces (B13) to $\epsilon_s = w_n/R$. Now, the substitution of (B12) and (B13) into (B9) and (B10) results in the relation between the stress and displacement:

$$N_{yy} = \frac{Eh}{1-\nu^2}\left(\frac{\partial w_y}{\partial y} + \nu\frac{w_n}{R}\right), \tag{B15}$$

$$N_{ss} = \frac{Eh}{1-\nu^2}\left(\frac{w_n}{R} + \nu\frac{\partial w_y}{\partial y}\right). \tag{B16}$$

Finally, the substitution of (B15) and (B16) into (B6) and (B8) results in the following equations:

$$\frac{E}{\rho_n(1-\nu^2)}\left(\frac{\partial^2 w_y}{\partial y^2} + \frac{\nu}{R}\frac{\partial w_n}{\partial y}\right) + \frac{q_y}{\rho_n h} = \frac{\partial^2 w_y}{\partial t^2}, \tag{B17}$$

$$-\frac{E}{\rho_n(1-\nu^2)}\left(\frac{w_n}{R^2} + \frac{\nu}{R}\frac{\partial w_y}{\partial y}\right) + \frac{q_n}{\rho_n h} = \frac{\partial^2 w_n}{\partial t^2}. \tag{B18}$$

Through these relations, the displacements (w_n and w_y) can be obtained if the external (surface) forces (q_y and q_n) are determined. The boundary conditions of (B17) and (B18) come from the fact that the nozzle is rigidly attached to the support ($w_y = w_n = 0$ at $y = L$) and is free at the tip ($N_{yy} = \partial w_y/\partial y + \nu w_n/R = 0$ at $y = 0$). All variables in (B17) and (B18) are then non-dimensionalized as follows:

$$\hat{y} = y/L, \quad \hat{t} = t/T_{acc}, \quad \hat{w}_y = w_y/R, \quad \hat{w}_n = w_n/R. \tag{B19a–d}$$

Substituting equation (B19*a–d*) into (B17) and (B18) leads to

$$\frac{\partial^2 \hat{w}_y}{\partial \hat{y}^2} + \frac{\nu L}{R}\frac{\partial \hat{w}_n}{\partial \hat{y}} + \hat{f}_y = \hat{T}\frac{\partial^2 \hat{w}_y}{\partial \hat{t}^2}, \tag{B20}$$

$$-\left(\frac{L}{R}\right)^2 \hat{w}_n - \frac{\nu L}{R}\frac{\partial \hat{w}_y}{\partial \hat{y}} + \hat{f}_n = \hat{T}\frac{\partial^2 \hat{w}_n}{\partial \hat{t}^2}. \tag{B21}$$

Here, $\hat{T}$ and $\hat{f}_i$ $(i = n, y)$ are dimensionless parameters, expressed as $\hat{T} = \rho_n(1-\nu^2)L^2/(ET_{acc}^2)$ and $\hat{f}_i = q_i(1-\nu^2)L^2/(ERh)$, respectively. Parameter $\hat{T}$ measures the relative contribution of the time-varying term $(\partial^2 \hat{w}_i/\partial \hat{t}^2)$ in both equations. For the present experiments, $\hat{T}$ is found to be negligible, $\hat{T} = \boldsymbol{O}(10^{-4})$, where $\rho_n = 1070$ kg m^{-3}, $L = 0.041$ m, $\nu = 0.55$, $E = 100$–270 kPa and $T_{acc} = 0.20$–0.43 s. The negligible contribution of the inertia term implies that the nozzle immediately reaches the quasi-equilibrium state, i.e. the deformation of the nozzle immediately conforms to the external forcing in y and n directions. Thus, the left-hand side of both equations can be ignored as follows:

$$\frac{\partial^2 \hat{w}_y}{\partial \hat{y}^2} + \frac{\nu L}{R}\frac{\partial \hat{w}_n}{\partial \hat{y}} + \hat{f}_y = 0, \tag{B22}$$

$$-\left(\frac{L}{R}\right)^2 \hat{w}_n - \frac{\nu L}{R}\frac{\partial \hat{w}_y}{\partial \hat{y}} + \hat{f}_n = 0. \tag{B23}$$

Integration of (B22) with $\hat{y}$ from 0 to y_p (an arbitrary vertical location on the nozzle) gives the following relation:

$$\left.\frac{\partial \hat{w}_y}{\partial \hat{y}}\right|_{\hat{y}=y_p} - \left.\frac{\partial \hat{w}_y}{\partial \hat{y}}\right|_{\hat{y}=0} + \frac{\nu L}{R}(\hat{w}_n|_{\hat{y}=y_p} - \hat{w}_n|_{\hat{y}=0}) + \int_0^{y_p} \hat{f}_y \,\mathrm{d}\hat{y} = 0. \tag{B24}$$

Applying the boundary condition at the nozzle tip $(\partial w_y/\partial y + \nu w_n/R = \partial \hat{w}_y/\partial \hat{y} + (\nu L/R)\hat{w}_n = 0)$, equation (B24) can be rewritten as (here, the subscript of $\hat{y} = y_p$ is neglected for convenience)

$$\frac{\partial \hat{w}_y}{\partial \hat{y}} = -\frac{\nu L}{R}\hat{w}_n - \int_0^{y_p} \hat{f}_y \,\mathrm{d}\hat{y} = 0. \tag{B25}$$

Now, the gradient of the displacement $(\partial w_y/\partial y)$ in (B23) can be replaced by the relation (B25):

$$\frac{L^2(1-\nu^2)}{R^2}\hat{w}_n - \frac{\nu L}{R}\int_0^{y_p} \hat{f}_y \,\mathrm{d}\hat{y} - \hat{f}_n = 0. \tag{B26}$$

Now, (B26) reveals that the normal displacement, $\hat{w}_n$, is directly determined by the external forces normal $(\hat{f}_n)$ and tangent $(\hat{f}_y)$ to the nozzle surface. Considering that the jet Reynolds number is of the order of 10^3, the contribution of friction is assumed to be negligible $(\hat{f}_y \simeq 0)$, which simplifies (B26) to $L^2(1-\nu^2)\hat{w}_n/R^2 = \hat{f}_n$. By the definition of $\hat{f}_n = q_n(1-\nu^2)L^2/(ERh)$ and the fact that the normal stress corresponds to the pressure difference between the nozzle wall (p) due to the jet acceleration (i.e. $p = q_n$), the pressure can be calculated as

$$\frac{R}{Eh}p = \hat{w}_n. \tag{B27}$$

Appendix C. Formulation of the potential energy stored by the flexible nozzle

This appendix presents the derivation of (4.17) in § 4.3. The elastic potential energy (P) is defined as the integration of the strain energy density (Z) along the nozzle volume (V), expressed as follows (Kraus 1967):

$$P = \int_V Z \,\mathrm{d}V. \tag{C1}$$

Here, the strain energy density is defined as $Z = 0.5\sigma_{ij}\epsilon_{ij}$, where σ_{ij} and ϵ_{ij} denote the stress and strain tensors, respectively, acting in the direction of the j axis on the surface normal to the i axis. The volume integration is performed as follows:.

$$P = \int_{-h/2}^{h/2} \int_0^L \int_0^{2\pi} \frac{1}{2}\sigma_{ij}\epsilon_{ij} R(1 + \zeta/R)\,\mathrm{d}\theta \mathrm{d}y\,\mathrm{d}\zeta. \tag{C2}$$

Since the axisymmetric deformation is dominant, the strain energy density can be approximated as $\sigma_{ij}\epsilon_{ij} \simeq \sigma_{ss}\epsilon_{ss}$, where $\epsilon_{ss} = w_n/R$ from (B13). Using the definition of the stress resultant ($N_{ss} = \int_{-h/2}^{h/2} \sigma_{ss}\,\mathrm{d}\zeta$), (C2) can be reduced to

$$P = \int_0^L \int_0^{2\pi} \frac{1}{2} N_{ss} w_n \,\mathrm{d}\theta\,\mathrm{d}y. \tag{C3}$$

Integral $\int_{-h/2}^{h/2} \sigma_{ij}\zeta\,\mathrm{d}\zeta$ was neglected since it is of $O(h^2)$. Equation (C3) is identical to (4.16). The relation between the stress resultant (N_{ss}) and the displacements (w_y and w_n) is given in (B15). Substitution of these into (C3) results in (C4):

$$P = \pi \frac{EhR}{1-\nu^2} \int_0^L \left(\frac{w_n}{R}\right)^2 \mathrm{d}y. \tag{C4}$$

Here, the normal displacement of the nozzle (w_n) can be estimated by the operation conditions using (4.6) in § 4.2 (which is rewritten as $\hat{w}_{n,max} = \rho_f u_t LD/(4EhT_{acc})$). Thus, the elastic potential energy can be finally obtained as follows:

$$P = \frac{\pi}{3(1-\nu^2)} \frac{\rho_f^2 u_t^2 R^3 L^3}{EhT_{acc}^2}. \tag{C5}$$

Appendix D. Calculation of the energy balance

In § 4.3, it was stated that the stored potential (elastic) energy is converted to kinetic energy of the jet during the contraction of the nozzle, expressed as follows:

$$\Delta M \sim P. \tag{D1}$$

Here, the increase in the kinetic energy of the jet (ΔM) is given as $\Delta(\rho_f \pi R^2 L u^2/2) = \rho_f \pi R^2 L(u\Delta u)$, and P comes from (4.17). Thus, (D1) can be rewritten as follows:

$$\rho_f \pi R^2 L(u\Delta u) \sim \frac{\pi R^3 a^2 \rho_f^2 L^3}{3(1-\nu^2)Eh}. \tag{D2}$$

If (D2) is divided by u_t^2 and is rearranged with respect to $\Delta u/u$, the following relation appears:

$$\frac{\Delta u}{u} \sim \frac{\rho_f R L^2}{3(1-\nu^2)EhT_{acc}^2} = \frac{1}{3(1-\nu^2)}\frac{\rho_f u_t^2 R}{Eh}\frac{L^2}{u_t^2 T_{acc}^2}. \tag{D3}$$

Recalling the dimensionless parameters, the effective acceleration time (Π_0) and the effective nozzle stiffness (Π_1), (D3) is modified into the following equation:

$$\frac{\Delta u}{u} \sim \frac{\Pi_0^2}{\Pi_1} \sim \frac{1}{\hat{c}^2}. \tag{D4}$$

Similarly, (4.26) can be obtained from (4.25) in § 4.3. First, (4.25) reads as follows:

$$\Delta M \sim P\frac{T_{acc}}{T_{eff}}. \tag{D5}$$

Here, the reduced wave speed in the upward direction ($+y$) is expressed as $c_{r,u} = u_t(1 - \sqrt{\Pi_1/2}) = -u_t(\sqrt{\Pi_1/2} - 1)$ since $\Pi_1 > 2$ in general. The substitution of ΔM, P and c_r into (D5) gives

$$\rho_f \pi R^2 L(u\Delta u) \sim \frac{\pi R^3 a^2 \rho_f^2 L^3}{3(1-\nu^2)Eh}\frac{T_{acc}u_t(\sqrt{\Pi_1/2}-1)}{L}. \tag{D6}$$

Again, (D6) is rewritten with respect to $\Delta u/u$:

$$\frac{\Delta u}{u} \sim \frac{1}{3(1-\nu^2)}\frac{\rho_f u_t R L}{T_{acc}Eh}(\sqrt{\Pi_1/2}-1) \sim \frac{\rho_f u_t^2 R}{Eh}\frac{L}{u_t T_{acc}}(\sqrt{\Pi_1/2}-1). \tag{D7}$$

Then, the substitution of the dimensionless parameters ($\Pi_0 = L/u_t T_{acc}$ and $\Pi_1 = Eh/(\rho_f u_t^2 R)$) results in (D8):

$$\frac{\Delta u}{u} \sim \frac{\sqrt{\Pi_1/2}-1}{\Pi_0\Pi_1}. \tag{D8}$$

Since Π_0^2/Π_1 scales with $1/\hat{c}^2$, the relation of $\Pi_0^2 \sim \hat{c}^2\Pi_1 \sim 1/\Pi_1$ holds when satisfying the optimal condition of $\hat{c} \simeq 3.0$. The substitution of $\Pi_0^2 \sim 1/\Pi_1$ into (B8) leads to the following:

$$\frac{\Delta u}{u} \sim \frac{\sqrt{\Pi_1/2}-1}{\sqrt{\Pi_1}} = \frac{1}{\sqrt{2}}\left(1 - \sqrt{\frac{2}{\Pi_1}}\right) \sim 1 - \sqrt{\frac{2}{\Pi_1}}. \tag{D9}$$

References

Abdelbaki, A.R., Paidoussis, M.P. & Misra, A.K. 2020 A nonlinear model for a hanging cantilevered pipe discharging fluid with a partially-confined external flow. *Intl J. Non-Linear Mech.* **118**, 103290.

Annus, I., Koppel, T., Sarv, L. & Ainola, L. 2013 Development of accelerating pipe flow starting from rest. *Trans. ASME J. Fluids Engng* **135**, 111204.

Arakeri, J.H., Das, D., Krothapalli, A. & Lourenco, L. 2004 Vortex ring formation at the open end of a shock tube: a particle image velocimetry study. *J. Phys. Fluids* **16**, 1008–1019.

Bergdorf, M., Koumoutsakos, P. & Leonard, A. 2007 Direct numerical simulations of vortex rings at $Re_\Gamma = 7500$. *J. Fluid Mech.* **581**, 495–505.

Bertram, C.D., Raymond, C.J. & Pedley, T.J. 1991 Application of nonlinear dynamics concepts to the analysis of self-excited oscillations of a collapsible tube conveying a fluid. *J. Fluid Struct.* **5**, 391–426.

BOUROUIBA, L., DEHANDSCHOEWERCKER, E. & BUSH, J.W. 2014 Violent expiratory events: on coughing and sneezing. *J. Fluid Mech.* **745**, 537–563.
BUJARD, T., GIORGIO-SERCHI, F. & WEYMOUTH, G.D. 2021 A resonant squid-inspired robot unlocks biological propulsive efficiency. *Sci. Robot.* **6**, eabd2971.
CHEN, S.S. & ROSENBERG, G.S. 1974 Free vibrations of fluid-conveying cylindrical shells. *ASME J. Engng Indus.* **96**, 420–426.
CHOI, H., LEE, J. & PARK, H. 2019 Wake structures behind a rotor with superhydrophobic-coated blades at low Reynolds number. *Phys. Fluids* **31**, 015102.
CHOI, D. & PARK, H. 2018 Flow around in-line sphere array at moderate Reynolds number. *Phys. Fluids* **30**, 097104.
CLIFFORD, A.A. 1973 *Multivariate Error Analysis: A Handbook of Error Propagation and Calculation in Many-Parameter Systems*. John Wiley & Sons.
DABIRI, J.O. 2009 Optimal vortex formation as a unifying principle in biological propulsion. *Annu. Rev. Fluid Mech.* **41**, 17–33.
DABIRI, J.O. & GHARIB, M. 2005 Starting flow through nozzles with temporally variable exit diameter. *J. Fluid Mech.* **538**, 111–136.
DAS, D., BANSAL, M. & MANGHNANI, A. 2017 Generation and characteristics of vortex rings free of piston vortex and stopping vortex effects. *J. Fluid Mech.* **811**, 138–167.
DAS, P., GOVARDHAN, R.N. & ARAKERI, J.H. 2018 Unsteady two-dimensional jet with flexible flaps at the channel exit. *J. Fluid Mech.* **845**, 462–498.
DAVID, M.J., GOVARDHAN, R.N. & ARAKERI, J.H. 2017 Thrust generation from pitching foils with flexible trailing edge flaps. *J. Fluid Mech.* **828**, 70–103.
DAZIN, A., DUPONT, P. & STANISLAS, M. 2006 Experimental characterization of the instability of the vortex rings. Part II: non-linear phase. *Exp. Fluids* **41**, 401–413.
DEWEY, P.A., BOSCHITSCH, B.M., MOORED, K.W., STONE, H.A. & SMITS, A.J. 2013 Scaling laws for the thrust production of flexible pitching panels. *J. Fluid Mech.* **732**, 29–46.
DIDDEN, N. 1979 On the formation of vortex rings: rolling-up and production of circulation. *Z. Angew. Math. Phys.* **30**, 101–116.
FANG, F., HO, K.L., RISTROPH, L. & SHELLEY, M.J. 2017 A computational model of the flight dynamics and aerodynamics of a jellyfish-like flying machine. *J. Fluid Mech.* **819**, 621–655.
FUKUMOTO, Y. & HATTORI, Y. 2005 Curvature instability of a vortex ring. *J. Fluid Mech.* **526**, 77–115.
GAO, L., WANG, X., SIMON, C.M. & CHYU, M.K. 2020 Development of the impulse and thrust for laminar starting jets with finite discharged volume. *J. Fluid Mech.* **902**, A27.
GARNIER, E. 2015 Flow control by pulsed jet in a curved S-duct: a spectral analysis. *AIAA J.* **53**, 2813–2827.
GHARIB, M., RAMBOD, E. & SHARIFF, K. 1998 A universal time scale for vortex ring formation. *J. Fluid Mech.* **360**, 121–140.
GOSLINE, J.M. & DEMONT, M.E. 1985 Jet-propelled swimming in squids. *Sci. Am.* **252**, 96–103.
HALDANE, D.W., PLECNIK, M.M., YIM, J.K. & FEARING, R.S. 2016 Robotic vertical jumping agility via series-elastic power modulation. *Sci. Robot.* **1**, eaag2048.
HATTORI, Y. & FUKUMOTO, Y. 2003 Short-wavelength stability analysis of thin vortex rings. *Phys. Fluids* **15**, 3151–3163.
HEIL, M. 1997 Stokes flow in collapsible tubes: computation and experiment. *J. Fluid Mech.* **353**, 285–312.
HEIL, M. & BOYLE, J. 2010 Self-excited oscillations in three-dimensional collapsible tubes: simulating their onset and large-amplitude oscillations. *J. Fluid Mech.* **652**, 405–426.
HEIL, M. & WATERS, S.L. 2006 Transverse flows in rapidly oscillating elastic cylindrical shells. *J. Fluid Mech.* **547**, 185–214.
HIBBELER, R.C. 2013 *Statics and Mechanics of Materials*. Pearson.
HIGHAM, T.E. & IRSCHICK, D.J. 2013 Springs, steroids, and slingshots: the roles of enhancers and constraints in animal movement. *J. Comput. Physiol.* B **183**, 583–595.
JUNG, C., SONG, M. & KIM, D. 2021 Starting jet formation through eversion of elastic sheets. *J. Fluid Mech.* **924**, A7.
KANG, C.K., AONO, H., CESNIK, C. & SHYY, W. 2011 Effects of flexibility on the aerodynamic performance of flapping wings. *J. Fluid Mech.* **689**, 32–74.
KIM, D. & GHARIB, M. 2011 Flexibility effects on vortex formation of translating plates. *J. Fluid Mech.* **677**, 255–271.
KRAUS, H. 1967 *Thin Elastic Shells: An Introduction to the Theoretical Foundations and the Analysis of their Static and Dynamic Behavior*. Wiley.
KRIEG, M. & MOHSENI, K. 2013 Modelling circulation, impulse and kinetic energy of starting jets with non-zero radial velocity. *J. Fluid Mech.* **719**, 488–526.

KRIEG, M. & MOHSENI, K. 2015 Pressure and work analysis of unsteady, deformable, axisymmetric, jet producing cavity bodies. *J. Fluid Mech.* **769**, 337–368.
KRUEGER, P.S. & GHARIB, M. 2003 The significance of vortex ring formation to the impulse and thrust of a starting jet. *Phys. Fluids* **15**, 1271–1281.
KUMARAN, V. 1998 Stability of the flow of a fluid through a flexible tube at intermediate Reynolds number. *J. Fluid Mech.* **357**, 123–140.
LAMB, H. 1945 *Hydrodynamics*. Dover.
LAWSON, N.J., RUDMAN, M., GUERRA, A. & LIOW, J.L. 1999 Experimental and numerical comparisons of the break-up of a large bubble. *Exp. Fluids* **26**, 524–534.
LI, H., CHOI, J., LI, B., KIM, I. & HEO, J. 2016 Numerical analysis on the gas flow dynamics from a rectangular slot-nozzle for pulse cleaning of filter unit. *Powder Technol.* **297**, 330–339.
LI, G., JAIMAN, R.K. & KHOO, B.C. 2021 Flow-excited membrane instability at moderate Reynolds numbers. *J. Fluid Mech.* **929**, A40.
LIMBOURG, R. & NEDIĆ, J. 2021*a* Formation of an orifice-generated vortex ring. *J. Fluid Mech.* **913**, A29.
LIMBOURG, R. & NEDIĆ, J. 2021*b* An extension to the universal time scale for vortex ring formation. *J. Fluid Mech.* **915**, A46.
LIN, T.C. & MORGAN, G.W. 1956 Wave propagation through fluid contained in a cylindrical, elastic shell. *J. Acoust. Soc. Am.* **28**, 1165–1176.
LINDEN, P.F. 2011 The efficiency of pulsed-jet propulsion. *J. Fluid Mech.* **668**, 1–4.
LOVE, A.E.H. 1888 The small free vibrations and deformation of a thin elastic shell. *Phil. Trans. R. Soc. Lond.* **179**, 491–546.
MAENG, H. & PARK, H. 2021 An experimental study on the heat transfer by a single bubble wake rising near a vertical heated wall. *Intl J. Heat Mass Transfer* **165**, 120590.
MARAIS, C., THIRIA, B., WESFREID, J.E. & GODOY-DIANA, R. 2012 Stabilizing effect of flexibility in the wake of a flapping foil. *J. Fluid Mech.* **710**, 659–669.
MEDINA, C. & KANG, C.K. 2018 An analytical solution to the aeroelastic response of a two-dimensional elastic plate in axial potential flow. *J. Fluid Mech.* **845**, R3.
MITTAL, R. 2018 Matters of the heart. *J. Fluid Mech.* **844**, 1–4.
MITTAL, R., NI, R. & SEO, J.H. 2020 The flow physics of COVID-19. *J. Fluid Mech.* **894**, F2.
MOSLEMI, A.A. & KRUEGER, P.S. 2010 Propulsive efficiency of a biomorphic pulsed-jet underwater vehicle. *Bioinspir. Biomim.* **5**, 036003.
MOSLEMI, A.A. & KRUEGER, P.S. 2011 The effect of Reynolds number on the propulsive efficiency of a biomorphic pulsed-jet underwater vehicle. *Bioinspir. Biomim.* **6**, 026001.
NICHOLS, J.T. & KRUEGER, P.S. 2012 Effect of vehicle configuration on the performance of a submersible pulsed-jet vehicle at intermediate Reynolds number. *Bioinspir. Biomim.* **7**, 036010.
PAAK, M., PAÏDOUSSIS, M.P. & MISRA, A.K. 2013 Nonlinear dynamics and stability of cantilevered circular cylindrical shells conveying fluid. *J. Sound Vib.* **332**, 3474–3498.
PACKARD, A. 1969 Jet propulsion and the giant fibre response of Loligo. *Nature* **221**, 875–877.
PAÏDOUSSIS, M.P. 1998 *Fluid-Structure Interactions: Slender Structures and Axial Flow*, vol. 1. Academic Press.
PAÏDOUSSIS, M.P. & DENISE, J.P. 1972 Flutter of thin cylindrical shells conveying fluid. *J. Sound Vib.* **20**, 9–26.
PARK, S.G., CHANG, C.B., HUANG, W.X. & SUNG, H.J. 2014 Simulation of swimming oblate jellyfish with a paddling-based locomotion. *J. Fluid Mech.* **748**, 731–755.
PARK, Y.J., JEONG, U., LEE, J., KWON, S.R., KIM, H.Y. & CHO, K.J. 2012 Kinematic condition for maximizing the thrust of a robotic fish using a compliant caudal fin. *IEEE Trans. Robot.* **28**, 1216–1227.
PARK, H., PARK, Y.J., LEE, B., CHO, K.J. & CHOI, H. 2016 Vortical structures around a flexible oscillating panel for maximum thrust in a quiescent fluid. *J. Fluid Struct.* **67**, 241–260.
PODOPROSVETOVA, A. & VEDENEEV, V. 2022 Axisymmetric instability of elastic tubes conveying power-law fluids. *J. Fluid Mech.* **941**, A61.
QUINN, D.B., LAUDER, G.V. & SMITS, A.J. 2014 Scaling the propulsive performance of heaving flexible panels. *J. Fluid Mech.* **738**, 250–267.
QUINN, D.B., LAUDER, G.V. & SMITS, A.J. 2015 Maximizing the efficiency of a flexible propulsor using experimental optimization. *J. Fluid Mech.* **767**, 430–448.
RENDA, F., SERCHI, F.G., BOYER, F. & LASCHI, C. 2015 Structural dynamics of a pulsed-jet propulsion system for underwater soft robots. *Intl J. Adv. Robot. Syst.* **12**, 68.
SAFFMAN, P.G. 1970 The velocity of viscous vortex rings. *Stud. Appl. Maths* **49**, 371–380.
SAFFMAN, P.G. 1995 *Vortex Dynamics*. Cambridge University Press.
SCARANO, F. 2001 Iterative image deformation methods in PIV. *Meas. Sci. Technol.* **13**, R1.

SHAPIRO, A.H. 1977 Steady flow in collapsible tubes. *Trans ASME J. Biomech. Engng* **99**, 126–147.
SIEKMANN, J. 1963 On a pulsating jet from the end of a tube. With application to the propulsion of certain aquatic animals. *J. Fluid Mech.* **15**, 399–418.
SIVIGLIA, A. & TOFFOLON, M. 2014 Multiple states for flow through a collapsible tube with discontinuities. *J. Fluid Mech.* **761**, 105–122.
STEWART, P.S. 2017 Instabilities in flexible channel flow with large external pressure. *J. Fluid Mech.* **825**, 922–960.
SULLIVAN, I.S., NIEMELA, J.J., HERSHBERGER, R.E., BOLSTER, D. & DONNELLY, R.J. 2008 Dynamics of thin vortex rings. *J. Fluid Mech.* **609**, 319–347.
SUTHERLAND, K.R. & MADIN, L.P. 2010 Comparative jet wake structure and swimming performance of salps. *J. Expl Biol.* **213**, 2967–2975.
TRIANTAFYLLOU, G.S., TRIANTAFYLLOU, M.S. & GROSENBAUGH, M.A. 1993 Optimal thrust development in oscillating foils with application to fish propulsion. *J. Fluid Struct.* **7**, 205–224.
WEYMOUTH, G.D. & TRIANTAFYLLOU, M.S. 2013 Ultra-fast escape of a deformable jet-propelled body. *J. Fluid Mech.* **721**, 367–385.
WHITTAKER, R.J., HEIL, M., JENSEN, O.E. & WATERS, S.L. 2010 Predicting the onset of high-frequency self-excited oscillations in elastic-walled tubes. *Proc. R. Soc.* A **466**, 3635–3657.
WHITTLESEY, R.W. & DABIRI, J.O. 2013 Optimal vortex formation in a self-propelled vehicle. *J. Fluid Mech.* **737**, 78–104.
WIDNALL, S.E., BLISS, D.B. & TSAI, C.Y. 1974 The instability of short waves on a vortex ring. *J. Fluid Mech.* **66**, 35–47.
WIDNALL, S.E. & SULLIVAN, J.P. 1973 On the stability of vortex rings. *Proc. R. Soc. Lond.* A **332**, 335–353.
ZHANG, S., LUO, X. & CAI, Z. 2018 Three-dimensional flows in a hyperelastic vessel under external pressure. *Biomech. Model. Mechanobiol.* **17**, 1187–1207.
ZHANG, K. & RIVAL, D.E. 2020 On the dynamics of unconfined and confined vortex rings in dense suspensions. *J. Fluid Mech.* **902**, A6.
ZHAO, W., FRANKEL, S.H. & MONGEAU, L.G. 2000 Effects of trailing jet instability on vortex ring formation. *Phys. Fluids* **12**, 589–596.